Mott glass to superfluid transition for random bosons in two dimensions

S. Iyer, D. Pekker, and G. Refael

A Mott Glass to Superfluid Transition for Random Bosons in Two Dimensions

S. Iyer, D. Pekker, and G. Refael

Department of Physics, California Institute of Technology,
MC 149-33, 1200 E. California Blvd., Pasadena, CA 91125
(Dated: January 30, 2012)

We study the zero temperature superfluid-insulator transition for a two-dimensional model of interacting, lattice bosons in the presence of quenched disorder and particle-hole symmetry. We follow the approach of a recent series of papers by Altman, Kafri, Polkovnikov, and Refael, in which the strong disorder renormalization group is used to study disordered bosons in one dimension. Adapting this method to two dimensions, we study several different species of disorder and uncover universal features of the superfluid-insulator transition. In particular, we locate an unstable finite disorder fixed point that governs the transition between the superfluid and a gapless, glassy insulator. We present numerical evidence that this glassy phase is the incompressible Mott glass and that the transition from this phase to the superfluid is driven by percolation-type process. Finally, we provide estimates of the critical exponents governing this transition.

PACS numbers:

I. INTRODUCTION

In the 1980s, seminal experiments on helium adsorbed in Vycor first attracted the attention of theorists to the random boson problem[1,2]. The onset of superfluidity in this disordered system showed, in some respects, striking similarities to ideal Bose gas behavior. Thus, in the decade before the realization of Bose-Einstein condensation in cold atomic gases, disordered bosonic systems were actually proposed as possible realizations of this elusive phenomenon. While studies of disordered bosons did not ultimately lead to the observation of Bose-Einstein condensation, the random boson problem continued to stimulate theoretical activity because of its considerable richness. The interplay of interactions and disorder leads to a variety of phases in bosonic systems; the description of these phases and the transitions between them is an ongoing challenge[3,4].

The theoretical investigation of random bosons in one dimension was pioneered by Giamarchi and Schulz, who described the transition to superfluidity in the presence of perturbatively weak disorder[5]. Subsequently, Fisher, Weichman, Grinstein, and Fisher expanded upon the work of Giamarchi and Schulz by establishing the now canonical zero temperature phase diagram of the Bose-Hubbard model with chemical potential disorder. The superfluid and Mott insulating phases of the clean model are separated by another insulating phase, the Bose glass. In this glassy phase, there exist rare-regions in which the energetic gap for adding another boson to the system vanishes. However, any additional bosons are localized by the disordered environment, rendering the phase a gapless, compressible insulator. Fisher et al. argued that there should be no direct superfluid-Mott insulator transition in the presence of quenched, uncorrelated disorder, or in other words, that the Bose glass *always* intervenes between the phases of the clean model[4]. The general picture formulated by these authors has been vindicated by over two decades of subsequent theoretical and numerical

work[6]. On the experimental front, following the observation of the Mott insulator to superfluid transition in cold atomic gases by Greiner et al.[7], there has been progress towards the realization of a Bose glass, including suggestive but inconclusive evidence that the phase has already been observed[8–11].

Meanwhile, evidence has accumulated that disordered bosonic systems may exhibit more exotic glassy phases in the presence of particle-hole symmetry. One such phase, the so-called Mott glass, differs from the Bose glass in that it is incompressible. This phase was originally proposed for systems of disordered fermions by Giamarchi, Le Doussal, and Orignac, but these authors predicted that it can exist in bosonic systems as well[12]. Subsequently, Altman, Kafri, Polkovnikov, and Refael studied a variant of the Bose-Hubbard model in which chemical potential disorder is omitted in favor of strong disorder in the on-site interaction and hopping. In the limit of large, commensurate boson filling, this model is equivalent to a chain of quantum rotors that can describe a Josephson junction array. Relative to the large filling, this rotor model exhibits an exact particle-hole symmetry which has important consequences for the phase diagram. Through a strong disorder renormalization group analysis, Altman et al. found that this symmetry results in the appearance of a Mott glass phase in this model[13]. The same authors later considered a generalization of this rotor model which allows for random offsets in the filling, effectively reintroducing a chemical potential. Generic disorder in the random offsets violates the particle-hole symmetry, and in this case, the rotor model exhibits the usual Bose glass phase[14,15]. This breakdown of the Mott glass demonstrates the link between exotic phases and symmetries of the disordered Hamiltonian. Irrespective of the identity of the glassy phase, Altman et al. also found that the superfluid-insulator transition at strong disorder lives in a different universality class from the weak disorder transition of Giamarchi and Schulz[13,14].

In this paper, we study the two-dimensional analogue

of the rotor model considered by Altman et al. in order to investigate the particle-hole symmetric random boson problem in $d > 1$. One of our goals is to look for the Mott glass, but more generally, we aim to characterize the phases and the superfluid-insulator transition of our model. Like Altman et al., the tool we use to do this is the strong disorder real space renormalization group (RG), first formulated by Ma and Dasgupta[16] to study the 1D Heisenberg antiferromagnet about thirty years ago. A numerical application of the RG by Bhatt and Lee followed shortly thereafter[17], and the method was later expanded upon and applied to more general spin models by Daniel Fisher[18]. Strong disorder renormalization has proven to be a powerful tool in the analysis of several disordered systems, especially in one dimension. In higher dimensions, application of the RG has been rarer, because in addition to the generic intractability of analytical approaches[19], there are few known transitions that exhibit so-called *infinite randomness*, a property that guarantees that the RG becomes asymptotically exact near criticality. The random boson model is not expected to exhibit infinite randomness, and indeed, the numerical data we present in this paper is consistent with this expectation. Hence, in addition to physical questions about the phases and phase transitions of the model, our work also aims to address a methodological question: might the strong disorder RG give useful information about a model, even when confronted with the twin difficulties of higher dimensionality and the absence of infinite randomness?

Summary of the Results

Our main results are as follows: we present numerical evidence for the existence of an unstable finite disorder fixed point of the RG flow, near which the distributions of Josephson couplings J_{jk} and charging energies U_j in the rotor model flow to universal forms. A schematic picture of this unstable fixed point and the flows in its vicinity is given in Figure 1.

To the left of the diagram, flows propagate towards a regime in which the ratio of $\bar{J}$, the mean of the Josephson couplings, to $\bar{U}$, the mean of the charging energies, vanishes; meanwhile, the ratio of ΔJ, the width of the Josephson coupling distribution, to $\bar{J}$ grows very large. These flows terminate in one of two insulating phases. The first is a conventional Mott insulator, in which it is energetically unfavorable for the particle number to fluctuate from the large filling at any site. The other is a glassy phase, in which there exist rare-regions of superfluid ordering. As the thermodynamic limit is approached, arbitrarily large rare-regions appear, driving the gap for charging the system to zero. However, the density of the largest clusters decays exponentially in their size, and the size of the largest cluster in a typical sample does not scale extensively in the size of the system. Moreover, the largest clusters are so rare that
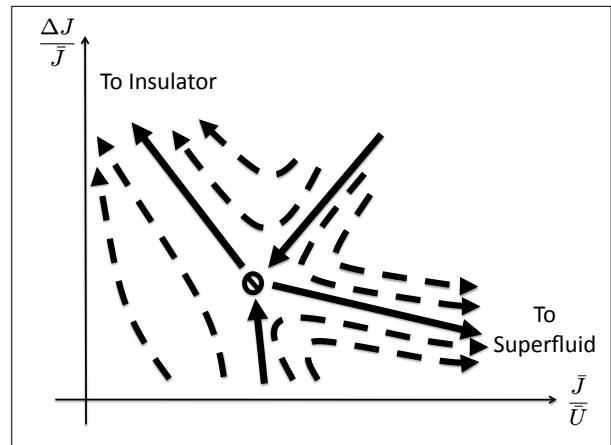

FIG. 1: A schematization of the universal features of the proposed flow diagram. The x-axis gives the ratio of the mean of the renormalized Josephson coupling distribution to the mean of the renormalized charging energy distribution. The y-axis gives the ratio of the standard deviation of the Josephson coupling distribution to its mean. In this context, the Josephson coupling distribution only includes the dominant $2\tilde{N}$ couplings in the renormalized J distribution, where $\tilde{N}$ is the number of sites remaining in an effective, renormalized lattice. See the text of Section III for the reasoning behind the exclusion of weaker Josephson couplings from statistics.

they cannot generate a finite compressibility. Thus, the phase is a Mott glass.

This insulating phase gives way to global superfluidity when the rare-regions of superfluid ordering percolate, producing a macroscopic cluster of superfluid ordering. The appearance of the macroscopic cluster is associated with flows that propagate towards the lower right of Figure 1, indicating that the unstable fixed point governs the glass-superfluid transition. Our numerical implementation of the strong disorder RG allows us to extract estimates for the critical exponents that characterize this transition. We are thus able to construct a compelling picture of the superfluid-insulator transition: a picture that must, however, be checked by other methods because of the perils of employing the strong disorder RG method in the vicinity of a finite disorder fixed point.

Organization of the Paper

We begin our analysis of the disordered rotor model in Section II by introducing the model, noting its relationship to the standard disordered Bose-Hubbard model and its special symmetries. We also discuss the clean limit and the disordered problem in one dimension. Section III is devoted to a description of the strong disorder renormalization group, as applied to the disordered rotor model. In discussing the method, we emphasize the adaptations needed to use the technique in dimensions greater than one. We then present data collected

from our numerical implementation of the strong disorder renormalization procedure in Section IV and subsequently explore what the data can tell us about the zero temperature phases and quantum phase transitions of our random boson model in Section V. In Section VI, we summarize the results, make connections to experiments, and give an outlook.

II. THE MODEL

In motivating the model that we study in this paper, we begin by writing down a disordered Bose-Hubbard Hamiltonian that includes randomness in the interaction and hopping along with the usual chemical potential disorder:

$$
\hat{H}_{\text{bh}} = -\sum_{\langle jk \rangle} t_{jk}(\hat{a}_j^\dagger \hat{a}_k + \hat{a}_k^\dagger \hat{a}_j) + \sum_j U_j \hat{a}_j^\dagger \hat{a}_j(\hat{a}_j^\dagger \hat{a}_j - 1)
$$
$$
-\sum_j \mu_j \hat{a}_j^\dagger \hat{a}_j \tag{1}
$$

Here, the creation and annihilation operators satisfy bosonic commutation relations:

$$
[\hat{a}_j, \hat{a}_k^\dagger] = \delta_{jk} \tag{2}
$$

and the hopping is between all nearest-neighbor sites on an $L \times L$ square lattice with periodic boundary conditions. An alternative representation of this model is given by the number and phase operators:

$$
\hat{a}_j = e^{i\hat{\phi}_j}\sqrt{\hat{N}_j} \tag{3}
$$

$$
[\hat{\phi}_j, \hat{N}_k] = i\delta_{jk} \tag{4}
$$

In terms of these operators:

$$
\hat{H}_{\text{bh}} = -\sum_{\langle jk \rangle} t_{jk}\left(\sqrt{\hat{N}_j}e^{-i\hat{\phi}_j}e^{i\hat{\phi}_k}\sqrt{\hat{N}_k}\right.
$$
$$
\left. +\sqrt{\hat{N}_k}e^{-i\hat{\phi}_k}e^{i\hat{\phi}_j}\sqrt{\hat{N}_j}\right)
$$
$$
+\sum_j U_j(\hat{N}_j - 1)\hat{N}_j - \sum_j \mu_j \hat{N}_j \tag{5}
$$

To obtain a large, commensurate boson filling N_0, the chemical potential is tuned such that the on-site interaction and chemical potential terms are minimized for $\hat{N}_j = N_0$. This consideration fixes $\mu_j = (2N_0 - 1)U_j$. Then, if we expand the number operators around this large filling as $\hat{N}_j = N_0 + \hat{n}_j$, the Hamiltonian becomes:

$$
\hat{H}_{\text{bh}} = -\sum_{\langle jk \rangle} t_{jk}N_0 \left(\sqrt{1 + \frac{\hat{n}_j}{N_0}}e^{-i\hat{\phi}_j}e^{i\hat{\phi}_k}\sqrt{1 + \frac{\hat{n}_k}{N_0}}\right.
$$
$$
\left. +\sqrt{1 + \frac{\hat{n}_k}{N_0}}e^{-i\hat{\phi}_k}e^{i\hat{\phi}_j}\sqrt{1 + \frac{\hat{n}_j}{N_0}}\right)
$$
$$
+\sum_j U_j \hat{n}_j^2 + (\text{const.}) \tag{6}
$$

The operators $\hat{n}_j$ now correspond to the particle number deviations from the large filling N_0. As such, n_j can take on any integer value from $-N_0$ to ∞, but we assume that N_0 is so large that we can let n_j run from $-\infty$ to ∞. The same approximation allows us to drop subleading (in $\frac{1}{N_0}$) terms in the hopping. We finally define the couplings $J_{jk} = 2t_{jk}N_0$ to arrive at the quantum rotor Hamiltonian:

$$
\hat{H} = -\sum_{\langle jk \rangle} J_{jk}\cos(\hat{\phi}_j - \hat{\phi}_k) + \sum_j U_j \hat{n}_j^2 \tag{7}
$$

This model, constructed as the large filling limit of a Bose-Hubbard Hamiltonian, can also be viewed as a description of a two-dimensional array of superconducting islands connected by Josephson junctions[13,14]. Moreover, Vosk and Altman have recently demonstrated that the one-dimensional model is relevant to cold atomic gases of rubidium-87[20].

When the Josephson couplings J_{jk} and charging energies U_j are uniform, the rotor model (7) exhibits a quantum phase transition between superfluid and Mott insulating phases at zero temperature. This transition is in the universality class of the three-dimensional classical XY model[3,4,21], and one recent study determines that the transition occurs at $\frac{J}{U} \approx 0.345$[22]. The critical exponent governing the divergence of the correlation length at the clean transition is $\nu \approx 0.663$[23]. This exponent violates the Harris criterion:

$$
\nu d \geq 2 \tag{8}
$$

when $d = 2$. Violation of the Harris criterion generically indicates that disorder will either change the universality class of the clean transition or completely smear it away. In the former case, a Griffiths phase will separate the phases of the clean system[24,25]. The nature of this intervening phase depends upon the specific model in question, but it is generically insulating. In 1D at $T = 0$, Altman et al. found an incompressible Mott glass phase and a quantum phase transition of Kosterlitz-Thouless type between this glassy phase and the superfluid[13]. The RG fixed point that controls this transition actually occurs at a point in the flow diagram where all $U_j = 0$, meaning that the transition can be tuned by only varying the disorder in the Josephson couplings at arbitrarily weak interaction strength.

In our work, we introduce disorder by choosing the initial distributions of charging energies and Josephson couplings, $P_i(U)$ and $P_i(J)$ to have one of the following forms:

1. Gaussian distributions truncated at three standard deviations:

$$
P_i(x) \propto \exp\left[-\frac{(x - x_0)^2}{2\sigma_x^2}\right] \tag{9}
$$

for $x \in (x_0 - 3\sigma_x, x_0 + 3\sigma_x)$.

2. Power law distributions with upper and lower cutoffs:

$$P_i(x) = \frac{\eta + 1}{x_{\max}^{\eta+1} - x_{\min}^{\eta+1}} x^{\eta} \qquad (10)$$

for $x \in (x_{\min}, x_{\max})$.

3. Flat distributions with upper and lower cutoffs:

$$P_i(x) = \frac{1}{x_{\max} - x_{\min}} \qquad (11)$$

for $x \in (x_{\min}, x_{\max})$. Of course, this is just a power law with exponent $\eta = 0$.

4. "Bimodal" distributions consisting of two flat peaks centered at x_ℓ and x_h:

$$P_i(x) = \frac{1}{2\delta x} \qquad (12)$$

for $x \in (x_\ell - \frac{\delta x}{2}, x_\ell + \frac{\delta x}{2})$ and $x \in (x_h - \frac{\delta x}{2}, x_h + \frac{\delta x}{2})$.

All of these distributions have positive lower and upper cutoffs ($x_{\min}$ and $x_{\max}$ respectively) and have zero weight for x outside of these bounds. This restriction avoids the complications of frustration in the phase degrees of freedom and the pathologies of the particle sinks that result from on-site charging spectrums that are unbounded from below.

Even in the presence of disorder, the Hamiltonian (7) respects two important symmetries. First, there is the global U(1) phase rotation symmetry:

$$\hat{\phi}_j \rightarrow \hat{\phi}_j + \varphi \qquad (13)$$

This means that the Hamiltonian conserves total particle number:

$$\hat{n}_{\text{tot}} = \sum_j \hat{n}_j \qquad (14)$$

The model is also globally particle-hole symmetric:

$$\begin{aligned} \hat{n}_j &\rightarrow -\hat{n}_j \\ \hat{\phi}_j &\rightarrow -\hat{\phi}_j \end{aligned} \qquad (15)$$

The particle-hole symmetry exists because the chemical potential coupling to the true particle number $\hat{N}_j$ has been tuned precisely to the value that enforces the large, commensurate filling. If this chemical potential is allowed to deviate from this value, then it would manifest in a chemical potential coupling to the particle number fluctuation $\hat{n}_j$, or equivalently, in offsets to the large filling. Such terms are absent from our rotor Hamiltonian (7), but let us momentarily consider the on-site charging spectrum (as a function of n_j) in the general situation where a filling offset δn_j may be present:

$$E_j(n_j) = U_j(n_j - \delta n_j)^2 \qquad (16)$$

The integer value of n_j that minimizes this energy changes at half-integer δn_j. For sufficiently strong disorder in δn_j, the introduction of an arbitrarily small global chemical potential shift will bring a finite fraction of sites j arbitrarily close to these density changing points. Thus, a finite density of particles will be added to the system, making it compressible. Nevertheless, these particles will be localized by the disordered environment, leaving the system globally insulating. This is the mechanism behind the formation of the Bose glass[4]. The situation changes at two special particle-hole symmetric points. One occurs when δn_j is restricted to be integer or half-integer. Then, at the half-integer sites, there is a degeneracy in the charging spectrum:

$$E_j\left(\delta n_j - \frac{1}{2}\right) = E_j\left(\delta n_j + \frac{1}{2}\right) \qquad (17)$$

In the 1D model, Altman et al. showed that this degeneracy gives rise to a random singlet glass[14], but we will not explore this situation in this paper. Instead, we will focus on the other particle-hole symmetric point where $\delta n_j = 0$ for all sites j. Now, if the U_j are distributed such that $U_{\min} > 0$, the on-site charging spectrum always has a unique minimum that is protected by a gap. The usual mechanism for Bose glass formation is evaded, and this allows for the possibility of realizing more exotic glassy phases. Thus, the particle-hole symmetry is a crucial feature of our model that can influence the nature of the intervening glassy phase.

III. STRONG DISORDER RENORMALIZATION OF THE 2D DISORDERED ROTOR MODEL

As mentioned previously, the tool that we use to study the disordered rotor model is the strong disorder real space renormalization method. Here we briefly review the method and discuss its application to the model at hand.

At first glance, problems involving strong quenched disorder may appear to be substantially more complicated than their clean counterparts. However, one way to motivate the strong disorder renormalization procedure is to consider that, in some cases, strong disorder can actually serve as an advantage. In particular, disorder can make the problem of finding the quantum ground state of a model more local. Having identified the strongest of all the disordered couplings in the Hamiltonian, we can then use the assumption of strong disorder to argue that other couplings in the vicinity (in real space) of this dominant coupling are likely to be much weaker. This means that the ground state can locally be approximated by satisfying the dominant coupling. Other terms in the Hamiltonian can then be incorporated as corrections. Quite often, these other terms are treated by means of perturbation theory, but this need not always be the case. These corrections manifest as new couplings in the model,

and thus, the procedure yields a new effective Hamiltonian. Since part of the ground state is specified in this step, some degrees of freedom of the system are decimated away. By repeating the procedure, we can iteratively specify the entire ground state[16,17]. Moreover, we can examine the way in which the probability distributions of the disordered couplings flow as the renormalization proceeds. One possibility is that the the model looks more and more disordered at larger length scales near criticality. This is the case for random transverse field Ising models in one and two dimensions[19,26,27]. In such cases, the model flows towards infinite randomness, and the strong disorder renormalization group becomes asymptotically exact near criticality[18]. Of course, it is also possible to flow towards finite or weak disorder, and in these cases, the reliability of the RG is less clear. We discuss this issue extensively, as it pertains to the disordered rotor model, in Appendix D.

A. The Basic RG Steps

We now concretize these ideas by application to the rotor Hamiltonian (7). In our model of random bosons in 2D, there are two types of disordered couplings, namely charging energies and Josephson couplings. In each step of the renormalization, we identify the maximum of all of these couplings, which defines the RG scale:

$$\Omega = \max\left[\{U_j\}, \{J_{jk}\}\right] \qquad (18)$$

How we then proceed depends upon which type of coupling is dominant.

Site Decimation

Consider the case where the charging energy on site X is dominant. We define a local Hamiltonian in which this charging energy term is chosen to be the unperturbed piece. All Josephson couplings entering the corresponding site are considered to be perturbations:

$$\hat{H}_X = U_X \hat{n}_X^2 - \sum_k J_{Xk} \cos\left(\hat{\phi}_X - \hat{\phi}_k\right) \qquad (19)$$

Satisfying the dominant coupling means setting $n_X = 0$ to leading order. This defines a degenerate manifold of local ground states: $|0, \{n_k\}\rangle$. In these kets, the first term corresponds to zero number fluctuation on site X and the second specifies the number fluctuations on all sites connected to X by a Josephson coupling. The degenerate space is infinitely large, corresponding to all possible choices of $\{n_k\}$. However, all matrix elements of the perturbative Josephson couplings in this ground state manifold vanish. The leading corrections then come from second order degenerate perturbation theory, in which we calculate corrections coming from excited states:

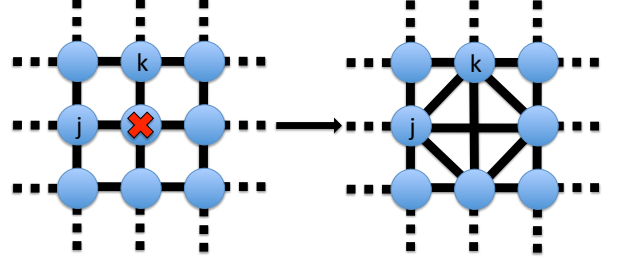$$|0, \{n_k\}\rangle' \approx |0, \{n_k\}\rangle \qquad (20)$$

FIG. 2: The site decimation RG step: The site marked with the X has the dominant charging energy and is decimated away, generating bonds between neighboring sites j and k with the effective coupling given in equation (21). The new local structure of the lattice is shown to the right.

$$+ \sum_{m \in k} \frac{J_{Xm}}{2U_X}\left(|1, n_m - 1\rangle + |-1, n_m + 1\rangle\right)$$

In the terms giving the perturbative corrections, we assume that the number fluctuations on all neighboring sites except m remain unmodified from their values in $\{n_k\}$. We next consider the matrix elements of these states in $\hat{H}_X$. Up to a constant term, these matrix elements are identically those that would result from an effective Josephson coupling:

$$\tilde{J}_{jk} = \frac{J_{jX} J_{Xk}}{U_X} \qquad (21)$$

between each two sites that were coupled to site X before the decimation step[13]. This process of site decimation is illustrated in Figure 2.

Link Decimation

Now, suppose that a Josephson coupling is the dominant energy scale. In this case, the local Hamiltonian is:

$$\hat{H}_{jk} = U_j \hat{n}_j^2 + U_k \hat{n}_k^2 - J_{jk} \cos\left(\hat{\phi}_j - \hat{\phi}_k\right) \qquad (22)$$

The local approximation to be made here is that, to lowest order, the phases on these adjacent sites should be locked together. In other words, the degree of freedom to be specified is the relative phase $\phi_j - \phi_k$. This motivates the introduction of new operators:

$$\hat{n}_C = \hat{n}_j + \hat{n}_k$$

$$\hat{\phi}_C = \frac{U_k \hat{\phi}_j + U_j \hat{\phi}_k}{U_j + U_k}$$

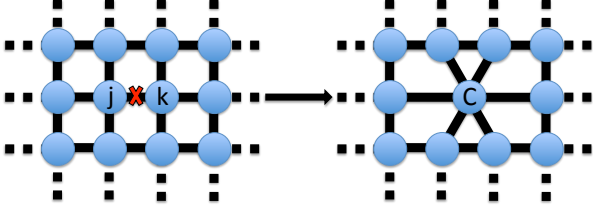$$\hat{n}_R = \frac{U_j \hat{n}_j - U_k \hat{n}_k}{U_j + U_k}$$

FIG. 3: The link decimation RG step: The crossed link has the dominant Josephson coupling. The two sites it joins are merged into one cluster, resulting the effective lattice structure shown to the right. The cluster C has an effective charging energy given in equation (26).

$$\hat{\phi}_R = \hat{\phi}_j - \hat{\phi}_k \qquad (23)$$

These operators satisfy the commutation relations:

$$[\hat{\phi}_C, \hat{n}_C] = i$$

$$[\hat{\phi}_R, \hat{n}_R] = i \qquad (24)$$

with all other commutators vanishing. Thus, the transformation preserves the algebra of number and phase operators. A subtlety arises for the relative coordinate operators $\hat{n}_R$ and $\hat{\phi}_R$ because, as defined above, n_R need not be an integer and $\phi_R \in [-2\pi, 2\pi)$ as opposed to $\phi_R \in [0, 2\pi)$. To deal with this difficulty, we may make the additional approximation of treating ϕ_R as a non-compact variable. This makes n_R continuous instead of discrete. Then, in terms of the new cluster and relative coordinate operators, the local Hamiltonian (22) reads:

$$\hat{H}_{jk} = \frac{U_j U_k}{U_j + U_k} \hat{n}_C^2 + (U_j + U_k)\hat{n}_R^2 - J_{jk} \cos\left(\hat{\phi}_R\right) \qquad (25)$$

To lowest order, we set $\phi_R = 0$. This decimation of the relative phase leaves the cluster phase ϕ_C unspecified, so two phase degrees of freedom have been reduced to one. The first term in $\hat{H}_{jk}$ shows that the inverse charging energies add like the capacitances of capacitors in parallel to give the charging energy for the cluster:

$$\tilde{U}_C = \frac{1}{\frac{1}{U_j} + \frac{1}{U_k}} = \frac{U_j U_k}{U_j + U_k} \qquad (26)$$

Figure 3 depicts this process of link decimation[13].

Higher order corrections to this picture, arising from harmonic vibrations of the phases that make up the cluster, can be obtained by considering the part of the local Hamiltonian involving the relative coordinate. These terms act approximately like a simple harmonic oscillator Hamiltonian on the basis of $\hat{n}_R$ eigenstates. Thus, the ground state for the relative coordinate can be approximated by a simple harmonic oscillator ground state:

$$|\psi_R\rangle \approx \frac{\gamma^{\frac{1}{8}}}{\pi^{\frac{1}{4}}} \int_{-\infty}^{\infty} dn_R \exp\left[-\frac{\gamma^{\frac{1}{2}}}{2} n_R^2\right] |n_R\rangle \qquad (27)$$

with:

$$\gamma = \frac{2(U_j + U_k)}{J_{jk}} \qquad (28)$$

This approximation is used in the numerics to compute *Debye-Waller factors* that modify Josephson couplings entering the newly formed cluster. Quantum fluctuations of ϕ_R weaken the phase coherence of the cluster, and consequently, suppress these Josephson couplings. Mathematically, the Debye-Waller factors arise because, in writing down the local, two site Hamiltonian (22), we have neglected that $\hat{\phi}_R$ also appears in the other links penetrating the two sites j and k. Consider a Josephson coupling from a third site m to the site j. This corresponds to a term in the full Hamiltonian (7):

$$\begin{aligned}
\cos\left(\hat{\phi}_m - \hat{\phi}_j\right) &= \cos\left(\hat{\phi}_m - \hat{\phi}_C - \mu_1\hat{\phi}_R\right) \\
&= \cos\left(\hat{\phi}_m - \hat{\phi}_C\right)\cos\left(\mu_1\hat{\phi}_R\right) \\
&\quad + \sin\left(\hat{\phi}_m - \hat{\phi}_C\right)\sin\left(\mu_1\hat{\phi}_R\right) \\
&\approx \cos\left(\hat{\phi}_m - \hat{\phi}_C\right)\langle\cos\left(\mu_1\hat{\phi}_R\right)\rangle + \\
&\quad \sin\left(\hat{\phi}_m - \hat{\phi}_C\right)\langle\sin\left(\mu_1\hat{\phi}_R\right)\rangle \quad (29)
\end{aligned}$$

with:

$$\mu_j = \frac{U_j}{U_j + U_k} \qquad (30)$$

The angle brackets in the final line of equation (29) refer to averages taken in the relative coordinate ground state (27). The expectation value of the sine vanishes, and the expectation value of the cosine yields the Debye-Waller factor:

$$c_{\mathrm{DW},j} \approx \frac{\sin^2(\pi\mu_j)}{\pi^2} \sum_{q=-\infty}^{\infty} \frac{(q^2 + \mu_j^2)}{(q^2 - \mu_j^2)^2} \exp\left(-\frac{\gamma^{\frac{1}{2}}}{4} q^2\right) \qquad (31)$$

In the numerics, we truncate the calculation of this sum at a specified order, $|q_{\mathrm{max}}| = 20$, and multiply the Josephson coupling J_{mj} by the result to find the new Josephson coupling $\tilde{J}_{mC}$ penetrating the cluster. Note that the Debye-Waller factor for links penetrating the site k is, in general, not equal to $c_{\mathrm{DW},j}$, but its calculation is completely analogous.

B. Adaptations for 2D

Sum Rule

As shown by Altman, Kafri, Polkovnikov, and Refael, the two renormalization steps outlined above form the basis of the strong disorder renormalization group for the disordered rotor model in 1D[13]. In higher dimensions,

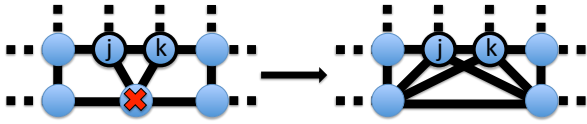FIG. 4: Site decimation with the sum rule: The site with the dominant charging energy (marked with an X) is coupled to two sites (j and k) that are already coupled to one another. After site decimation, the effective Josephson coupling between sites j and k is the sum of the old coupling and the effective coupling generated through decimation of site X (see equation (32)).
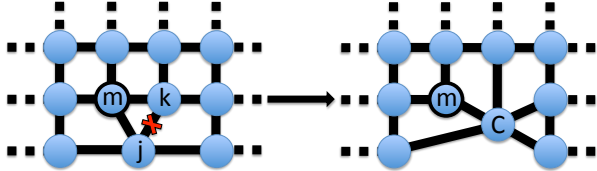

FIG. 5: Link decimation with the sum rule: The two sites connected by the dominant Josephson coupling (sites j and k) are both coupled to a third site m. Following link decimation, the effective Josephson coupling between site m and the cluster C is the sum of the two preexisting couplings between site m and sites j and k (see equation (33)), up to corrections coming rom Debye-Waller factors.

the geometry of the lattice changes as the renormalization proceeds, and this presents complications. For example, in Figure 4, decimation of a site X produces an effective Josephson coupling between two sites j and k that are already linked to one another by a preexisting Josephson coupling. In our numerics, we sum the preexisting and new coupling to form the effective coupling between the remaining sites:

$$\tilde{J}_{jk} = J_{jk} + \frac{J_{jX} J_{Xk}}{U_X} \qquad (32)$$

A similar situation can arise during link decimation. In Figure 5, a cluster is formed by two sites j and k, each of which is connected to a third site m. Up to corrections coming from Debye-Waller factors, the effective Josephson coupling joining site m to the cluster is:

$$\tilde{J}_{mC} = J_{mj} + J_{mk} \qquad (33)$$

Some authors replace the *sum rule* in equations (32) and (33) with a *maximum rule* [19,26,27]. The motivation behind the maximum rule is that, in the strong disorder limit:

$$\max\left[J_{jk}, \frac{J_{jX} J_{Xk}}{U_X}\right] \approx J_{jk} + \frac{J_{jX} J_{Xk}}{U_X} \qquad (34)$$

This should be a good approximation in an infinite disorder context. For our model however, we find that the sum rule increases the class of distributions which find the unstable fixed point depicted schematically in Figure 1. For further discussion of the difference between the sum and maximum rules, please consult Appendix A.

Thresholding

In dimensions greater than one, there is a tendency for the numerics to slow down considerably if the renormalization procedure involves a lot of site decimation. Again, the source of the problem is the evolution of the lattice under the RG. If a site X is decimated, then effective links are generated between each pair of sites that were previously coupled to X. Thus, site decimation generates many new couplings, increasing the coordination number of the effective lattice. At the same time, the site decimation step takes computer time quadratic in the coordination number of the site being decimated. To apply the procedure to large lattices, it is necessary to find a way to circumvent this difficulty.

At the beginning of the RG, we specify a thresholding parameter, which we call α. During a site decimation, if a new Josephson coupling is created between sites j and k such that:

$$\tilde{J}_{jk} = \frac{J_{jX} J_{Xk}}{U_X} < \alpha U_X = \alpha \Omega \qquad (35)$$

then the coupling is thrown away. For convenience in implementation, the new bond is ignored only if it does not sum with a preexisting Josephson coupling. If α is chosen to be very small, then ignoring the coupling will hopefully not affect the future course of RG. However, to be more careful, it is better to perform an extrapolation in the threshold α to see if the numerics converge. Using this thresholding procedure, we are able to reach lattices up to size 300×300, if we additionally require averaging over a reasonably large number of disorder samples. In this paper, unless otherwise stated, we always use 10^3 samples for any given choice of distributions.

Distribution Flows

Typically, in an application of the strong disorder renormalization method, it is interesting to monitor the flow of the distributions of the various couplings as the RG proceeds. This is straightforward for a 1D chain, but in higher dimensions, there is yet again a complication from the evolving lattice structure. As the renormalization proceeds, it is possible to generate very highly connected lattices. Many of the effective Josephson couplings will, however, be exceedingly small. Incorporating these anomalously small couplings into statistics can be misleading. Despite the large number of weak bonds, there may exist a number of strong bonds sufficient to produce superfluid clusters. In fact, including the weak bonds in statistics is analogous to polluting the statistics with the inactive next-nearest neighbor Josephson couplings in the original lattice. It is more appropriate to follow Motrunich et al. and focus on the largest $O(\tilde{N})$ Josephson couplings, where $\tilde{N}$ is the number of sites remaining in the effective lattice[27]. In the remainder of the
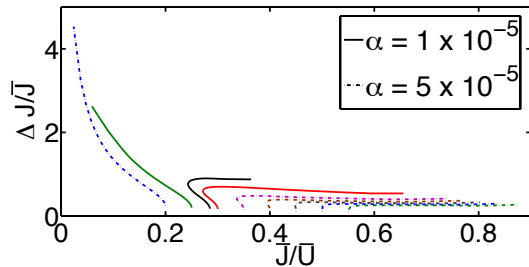
FIG. 6: The projection, in the $\Delta J/\bar{J}$ vs. $\bar{J}/\bar{U}$ plane, of the flows of the coupling distributions at different stages of the RG. The initial distributions $P_i(U)$ and $P_i(J)$ are both truncated Gaussians, and J_0 (the center of the initial J distribution) is used as the tuning parameter. Each flow corresponds to a different choice of the tuning parameter. The flows start at the bottom of the figure and go up and to the left or up and to the right. A smaller value of the thresholding parameter is used near criticality as indicated by the legend. All runs were done on $L = 100$ lattices.

paper, the "Josephson coupling distribution" will therefore refer solely to the dominant $2\tilde{N}$ effective Josephson couplings at any stage in the RG, and all statistics will be done only on these $2\tilde{N}$ couplings.

IV. NUMERICAL APPLICATION OF THE STRONG DISORDER RG

In this section, we present numerical data collected from our implementation of the strong disorder renormalization group. First, we explore the strong disorder RG flows of the distributions of charging energies and Josephson couplings. This investigation points to the existence of an unstable fixed point of the RG flow. We find that the presence of this fixed point is robust to many different changes in the choices of the initial distributions. Next, we examine the distributions generated by the RG near this fixed point and find that universal physics arises in its vicinity. Subsequently, we proceed away from the fixed point to study properties of the phases of the disordered rotor model. We find phases that we tentatively identify as Mott insulating, glassy, and superfluid, and furthermore, we find that the unstable fixed point governs the putative glass-superfluid transition. We defer detailed interpretation of the data and analysis of the transition to Section V.

A. Flow Diagrams and the Finite Disorder Fixed Point

In Figures 6-8, we plot flows of quantities that characterize the Josephson coupling and charging energy distributions. We emphasize again that, in the context of our study of distribution flows, the "Josephson coupling distribution" actually only includes the greatest $2\tilde{N}$ Joseph-
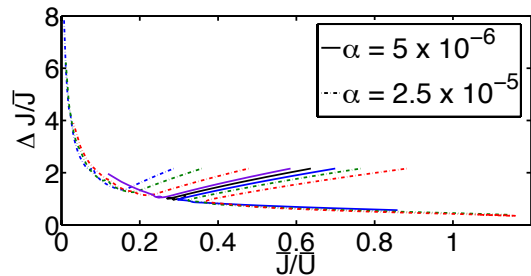

FIG. 7: Same as Figure 6, except $P_i(U)$ is Gaussian and $P_i(J) \propto J^{-1.6}$, with cutoffs chosen to make the latter distribution very broad. The parameter U_0 is used to tune through the transition. The flows begin near the center of the figure. To the left of the figure, flows initially propagate towards the bottom left but eventually turn around and propagate towards the top left. To the right of the figure, flows initially propagate towards the bottom left but eventually turn around and propagate towards the bottom right. All runs were done on $L = 300$ lattices.
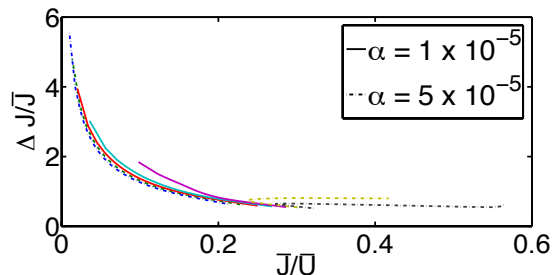

FIG. 8: Same as Figure 6, except $P_i(U) \propto U^5$ and $P_i(J) \propto J^{-3}$. The tuning parameter is $J_{\min}$, the lower cutoff of $P_i(J)$. All runs were done on $L = 150$ lattices.

son couplings, where $\tilde{N}$ is the number of sites remaining in the effective lattice. After M decimation steps of the RG, we stop the procedure and look at the remaining charging energies and these dominant Josephson couplings. We then use these values to update estimates for the mean and standard deviation corresponding to that step in the RG. For each realization of the randomness (i.e. each sample), we do this for many different choices of M, and we repeat the process for 10^3 realizations of the randomness. Ultimately, this procedure gives a "flow" that characterizes the disorder-averaged evolution of the distributions at different stages of the renormalization.

The x-axes of Figures 6-8 give the ratio of the means of the two distributions. Meanwhile, the y-axes give the ratio of the standard deviation of the Josephson coupling distribution to the mean of the distribution. The plots actually show 2D projections of flows that occur in the space of all possible distributions. At the very least, these plots imply the existence of a third axis, namely $\frac{\Delta U}{\bar{U}}$, which may carry important information. Nevertheless, these highly simplified 2D pictures are surprisingly effective in describing the fate of the model with different choices of parameters. In interpreting Figures 6-8, the

reader will likely find it helpful to glance back to Figure 1, which shows a schematization of the flows.

Figure 6 specifically corresponds to flows for initial distributions $P_i(U)$ and $P_i(J)$ that are Gaussian. The center of the Josephson coupling distribution is used as the tuning parameter. To the left of the plot are two flows that propagate to the top left of the diagram, towards small $\frac{\bar{J}}{U}$ and large $\frac{\Delta J}{J}$. Since these flows propagate towards high $\bar{U}$, it is tempting to identify them as flowing towards an insulating regime. Meanwhile, to the right of the plot, there are seven flows that propagate towards high $\bar{J}$, and it is tempting to identify these as propagating towards a superfluid regime. At the interface between these two behaviors, the flows "slow down" and travel a shorter distance in the plane. This behavior is suggestive of a separatrix flow that terminates at an unstable fixed point, as shown in Figure 1.

Our next goal will be to show that the behavior indicating the presence of this unstable fixed point is robust to changes in the choice of the initial distributions. In Figure 7, $P_i(U)$ is a Gaussian, and $P_i(J) \propto J^{-1.6}$. The center of the charging energy distribution, U_0, is used as the tuning parameter. The numerical choices place the flows initially above and to the right of the location of the unstable fixed point in the previous figure. From the point of view of the strong disorder RG procedure, this choice of initial distributions is advantageous, because the flows begin in a regime of high disorder in J, where the procedure is more accurate. Later in the paper, after presenting evidence of the universal physics that emerges in the disordered rotor model, we will focus on this choice of distributions exclusively. Therefore, we have collected additional details about these distributions in Appendix C. Note that the leftmost flows in Figure 7 initially propagate towards the lower left hand corner of the figure; then, they turn upward, continuing onward to lower $\frac{\bar{J}}{U}$ but now also towards high $\frac{\Delta J}{J}$. Hence, they share the same qualitative fate as the leftmost flows in Figure 6. To the right of Figure 7, the flows initially also propagate towards the lower left; however, these flows ultimately turn around and propagate towards high $\frac{\bar{J}}{U}$. The separatrix that divides these two classes of flows appears to terminate in the same critical region that was seen in Figure 6.

In Figure 8, we make yet another choice of initial distributions. Now, $P_i(J) \propto J^{-3}$ and $P_i(U) \propto U^5$. The resulting flow diagram again suggests the presence of an unstable fixed point in the same critical region. It would be misleading, however, to suggest that every flow diagram generated by the RG will have the nice properties of Figures 6-8. We provide a counterexample in Figure 9, in which $P_i(U)$ is bimodal and $P_i(J) \propto J^{-1.6}$. Panel (a) shows the extremely complicated behavior of some of the flows. These features are reflections of the structural details of the bimodal distribution. We will see shortly that, at least in the vicinity of criticality, the RG works to wash away these details and construct universal distributions. After these universal distributions are
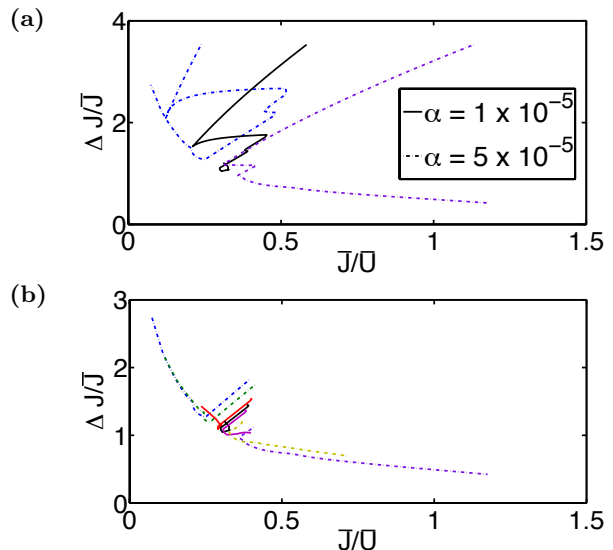

FIG. 9: In these numerical flow diagrams, $P_i(U)$ is bimodal and $P_i(J) \propto J^{-1.6}$, with cutoffs chosen to make the latter distribution very broad. In panel (a), we show a few sample flows that start near the top of the figure and initially propagate towards the lower left hand corner. The complex features of these flows reflect the structural details of the bimodal U distribution. In panel (b), we exhibit the flows at late RG times, when the procedure has had an opportunity to renormalize away the microscopic details of the initial distributions. Then, the flows are, at least qualitatively, more similar to those seen in Figure 7. All runs were done on $L = 200$ lattices.

somewhat well approximated, the flows should be more well behaved, but in Figure 9, we see a non-universal era of the flows, where the complexities of the initial distributions can manifest in complicated flows. To bring out this point more clearly, we have removed data for the early stages of the RG in panel (b). Now the "late RG-time" behavior of the flows falls more nicely in line with what is seen in Figure 7.

B. Universal Distributions

Near the unstable finite disorder fixed point of the RG flow, we expect universal physics to emerge. Certain aspects of the critical behavior should be independent of microscopic details, including the structure of the initial distributions. The universality of the fixed point should become evident in the forms of the *renormalized* distributions generated through the RG: whatever the initial distributions may be, they should evolve towards universal forms, provided that they put the system near criticality.

We first focus on determining the universal form of the fixed point Josephson coupling distribution. Figure 10 shows data for the four different choices of the initial distributions that we explore in this paper. In panels (a), (c), and (d), $P_i(U)$ and $P_i(J)$ have the same qualitative

form, and in panel (b), $P_i(J) \propto J^{-1.6}$ and $P_i(U) \propto U^{1.6}$. We tune the parameters characterizing the distributions such that the flows propagate near the unstable fixed point, run the numerics on 100×100 lattices, and plot the initial distributions alongside the renormalized distributions when 100 sites remain in the effective lattice. For the renormalized distributions, we again only include the dominant $2\tilde{N} = 200$ Josephson couplings for each sample. The renormalized distributions suggest that the RG indeed washes away the details of the initial choices, leaving a power law in each case. The universality of this power law is more striking in Figure 11, where we plot the renormalized distributions for the four cases together. In this plot, we scale J for each of the four cases by the mean RG scale Ω when only 100 sites remain. This scaling causes the distributions to nearly collapse onto one another, revealing the universal form:

$$P_{\text{univ}}\left(\frac{J}{\Omega}\right) \propto \left(\frac{J}{\Omega}\right)^{-\varphi} \qquad (36)$$

We will momentarily defer providing a numerical estimate of φ, in anticipation of presenting higher quality data, taken from runs on larger lattices, below.

We have not plotted the renormalized charging energy distributions for the four cases shown in Figure 10. Were we to do so, we would see that these distributions, while showing hints of universality, are not as strikingly universal as the corresponding renormalized Josephson coupling distributions. The reason for this is the following: in three out of the four cases, the initial distributions have $J_{\max} < U_{\max}$. Several of the initial distributions we study in this paper satisfy this property, because in dimensions greater than one, interesting choices of distributions typically have most bare charging energies greater than most bare Josephson couplings. Otherwise, they almost certainly yield superfluid behavior. Consequently, for three out of the four cases in Figure 10, the RG begins with only site decimations. These site decimations dramatically modify the Josephson coupling distribution, but the charging energy distribution is, to a large extent, only truncated from above by the renormalization scale. Later on in the procedure, after many sites have been decimated away, the RG enters a regime where the charging energy and Josephson coupling scales compete. Only then do link decimations begin to occur, and only then can the charging energy distribution begin to evolve in a nontrivial way. However, by this point, there is far less RG time remaining for the fixed point distribution to emerge.

There are two ways to circumvent this difficulty. One strategy is to note that this problem of insufficient RG time would not arise if we had access to arbitrarily large lattices. We could follow the renormalization as long as necessary to construct the universal distributions. Thus, we can try to explore larger lattices up to the limits set by our computational capabilities. On the other hand, another solution is to work with very wide initial distributions of Josephson couplings. These are distributions
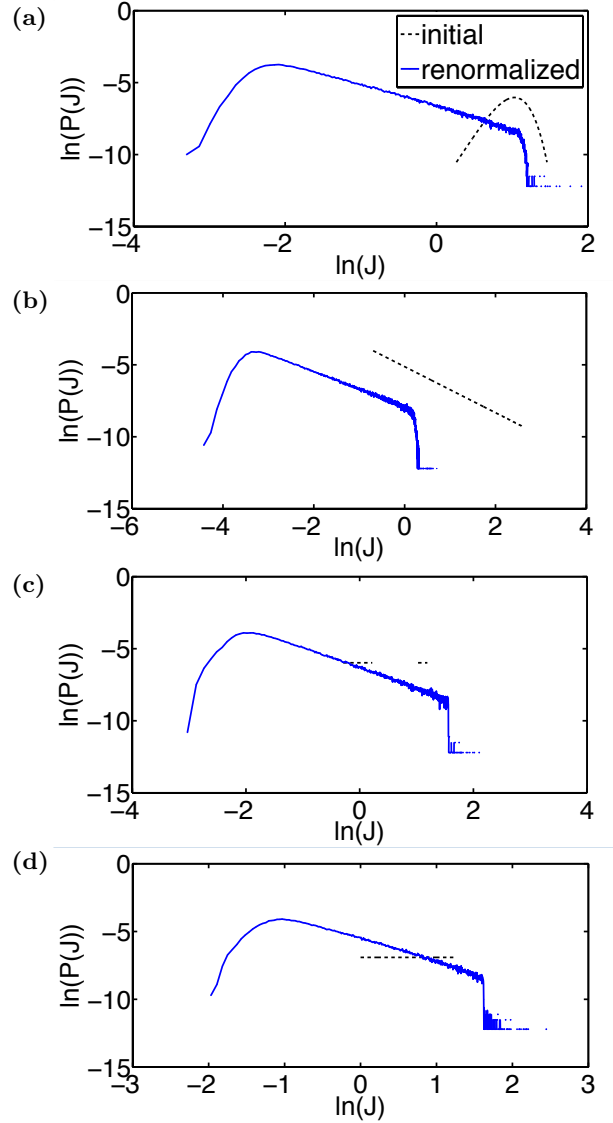

FIG. 10: Log-log plots of initial and renormalized Josephson coupling distributions for near-critical flows. All runs were done on $L = 100$ lattices with $\alpha = 5 \times 10^{-6}$. Each plot shows the initial distribution and the distribution when the effective lattice has 1% of the original number of sites. The initial distributions have four different forms, but the distributions after renormalization show a universal power law. Note that the plots of initial distributions in these plots were not constructed from actual data (i.e. actual numerical sampling of the distributions) but were instead constructed by hand.
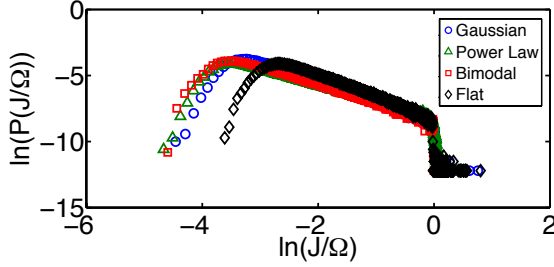
FIG. 11: The distributions from Figure 10, with the Josephson coupling strength scaled by the mean RG scale Ω at the corresponding stage of the RG. The near collapse of the distributions reveals the universal power law form of the Josephson coupling distribution near the unstable fixed point. A refined version of this plot, showing data for larger lattices (but also different choices of initial distributions), can be found in panel (b) of Figure 13.

which have large $\frac{\Delta J}{\bar{J}}$. As such, they correspond to flows that begin above the unstable fixed point in our $\frac{\Delta J}{\bar{J}}$ vs. $\frac{\bar{J}}{U}$ flow diagrams. Using such distributions, it is possible to engineer situations where most bare charging energies exceed most bare Josephson couplings but where, due to the presence of a small fraction of anomalously large Josephson couplings, $J_{\max} > U_{\max}$ at the beginning of the RG. If the parameters are chosen appropriately, the renormalization procedure will begin with a few link decimations, until the charging energy and Josephson coupling scales meet. After this point, the RG will feature an interplay of site and link decimations. Thus, both the Josephson coupling and charging energy distributions will evolve nontrivially.

To target the fixed point charging energy distribution, we apply both of the strategies. We proceed to 200×200 lattices and compute renormalized distributions when the effective lattice has 200 sites remaining. Additionally, we work with very wide initial Josephson coupling distributions. In order to achieve large initial $\frac{\Delta J}{\bar{J}}$, we restrict our attention to power law distributions of Josephson couplings of the form $P_i(J) \propto J^{-1.6}$. We vary the choice of the initial charging energy distribution and tune the parameters near criticality. The results are shown in Figure 12. Now, the RG does generate a universal form for the charging energy distribution, and in Figure 13, we scale the renormalized distributions by the corresponding RG scales to expose the universality more clearly. Figure 13 suggests that the functional form of the fixed point charging energy distribution may be:

$$P_{\mathrm{univ}}\left(\frac{U}{\Omega}\right) \propto \left(\frac{\Omega}{U}\right)^{\beta} \exp\left[-\left(\frac{g_U}{\Omega}\right) \times \left(\frac{\Omega}{U}\right)\right] \quad (37)$$

where g_U is an energy scale below which the charging energies are exponentially rare. We have been unable to extract a good estimate of β. Panel (a) of Figure 13 presupposes $\beta \approx 1$, and the linearity of the plots suggests

that this may be close to the actual value. Taking $\beta = 1$ and focusing on the case where $P_i(U)$ is Gaussian (because that is the choice of initial distributions for which we have most accurately targeted criticality), we fit:

$$\frac{g_U}{\Omega} \approx 0.66 \pm 0.02 \quad (38)$$

We should note that qualitatively similar charging energy distributions to those seen in Figure 12 still emerge near criticality if we relax the restrictions of initially power law J distributions and initially high $\frac{\Delta J}{\bar{J}}$. This is true of the distributions studied in Figure 10, even in the flat and bimodal cases where $J_{\max} < U_{\min}$ initially and clusters can only form due to the use of the sum rule. As argued above, the additional restrictions we impose on $P_i(J)$ in Figure 12 simply allow the RG to construct the fixed point distributions more cleanly.

In the lower panel of Figure 13, we additionally present data for the Josephson coupling distributions at the same stage of the RG. Again focusing on the data for the case where $P_i(U)$ is Gaussian, we can estimate:

$$\varphi \approx 1.15 \pm 0.01 \quad (39)$$

Before proceeding, we should note that the form of the fixed point J distribution allows us to construct an argument for the validity of the RG near criticality. We expand upon this argument greatly in Appendix D, but we will sketch the basic premise here. Essentially, we should consider the implications of the fixed point distributions for the reliability of each of the RG steps. The validity of site decimation rests on the reliability of the perturbative treatment of the Josephson couplings entering the site with the dominant charging energy. The form of the critical Josephson coupling distribution immediately guarantees that most Josephson couplings are much weaker than the RG scale. For the Gaussian case in Figure 13, the ratio of the median J to the RG scale is $\frac{J_{\mathrm{typ}}}{\Omega} \approx 0.11 \pm 0.01$. Hence, the site decimation is usually very safe. In the case of link decimation, a similar argument allows us to ignore, to leading order, other Josephson couplings penetrating the sites joined by the dominant coupling. However, the structure of the critical *charging energy* distribution, shown in Figure 13, actually suggests that there can be a large number of charging energies of the same order as the RG scale; in particular, the ratio of the median U to the RG scale is $\frac{U_{\mathrm{typ}}}{\Omega} \approx 0.67 \pm 0.01$. Consequently, the question of the reliability of link decimation reduces to the following: in a single junction (or two-site) problem, how reliable is cluster formation when both charging energies are weaker than the Josephson coupling but potentially of the same order-of-magnitude? We address this question in Appendix D and find that the link decimation step also seems to be reasonably safe.
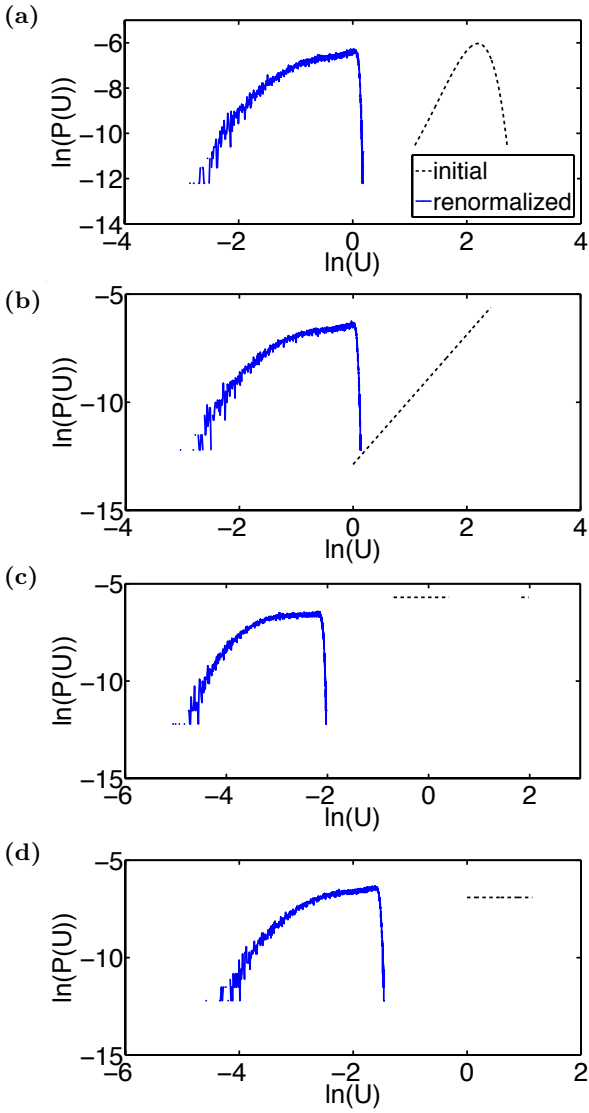
(a)

(b)

(c)

(d)

FIG. 12: Log-log plots of initial and renormalized charging energy distributions for near-critical flows. All runs were done on $L = 200$ lattices with $\alpha = 5 \times 10^{-6}$. Each plot shows the initial distribution and the distribution when the effective lattice has 0.5% of the original number of sites. The initial charging energy distributions have four different forms, but the distributions after renormalization show a universal form. Note that the plots of initial distributions in these plots were not constructed from actual data (i.e. actual numerical sampling of the distributions) but were instead constructed by hand.
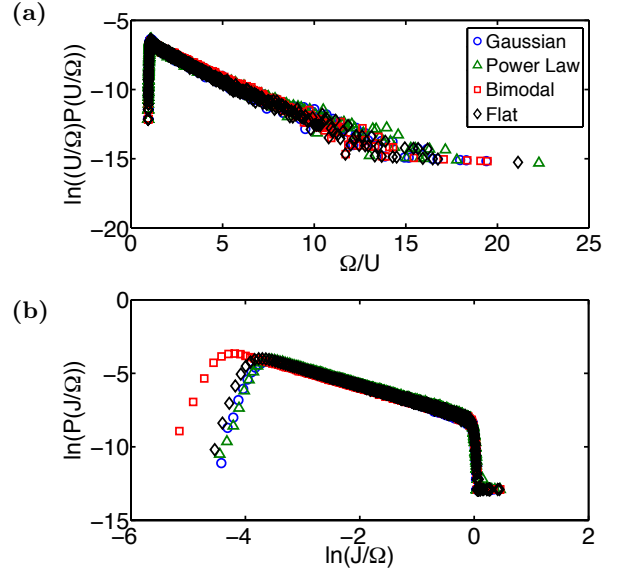

(a)

(b)

FIG. 13: In panel (a), the renormalized distributions from Figure 12 are plotted together, with the charging energies U scaled by the mean RG scale Ω. In panel (b), we provide a similar plot for the renormalized Josephson coupling distributions produced by the runs in Figure 12.

C. Physical Properties and Finite Size Scaling

To determine a preliminary classification of the phases of the model, we now measure four physical properties. First, we measure s_{max}, the size of the largest cluster formed by link decimations during the renormalization procedure. This corresponds to the largest domain of superfluid ordering in the system. We also measure s_2, the size of the second largest cluster. We will see that the behavior of this quantity differs dramatically from that of s_{max} in the superfluid phase, and therefore, both are interesting quantities to measure.

We also calculate the charging gap for the system, Δ_{min}. We can estimate this quantity by simply measuring the charging energy of the final site remaining in the RG.

Finally, we measure a susceptibility towards superfluid ordering. Consider adding a perturbation of the following form to the rotor model Hamiltonian:

$$\hat{H}' = -h \sum_j \cos(\hat{\phi}_j) \qquad (40)$$

In the RG, we can evaluate the linear response of the system to this perturbation and measure the susceptibility:

$$\chi = \frac{1}{L^2} \sum_j \frac{\partial \langle \cos \hat{\phi}_j \rangle}{\partial h} \bigg|_{h=0} \qquad (41)$$

The terms of this sum are computed during site decimation. Perturbation theory gives a single site susceptibility of $\frac{1}{U_X}$, where X is the site being decimated. Neglecting

corrections from harmonic fluctuations, we can find the contribution of a cluster to the susceptibility by multiplying the perturbative result by s^2, where s is the size of the cluster. One factor of s arises from the fact that the cluster represents s terms in the original sum (41), and the other follows from the fact that the effective field coupling to the cluster phase is enhanced s times when s phases rotate together. When harmonic fluctuations are taken into account, both of these factors of s should be replaced by a renormalized factor which we denote as b. This b-factor accounts for the fact that quantum fluctuations weaken the phase coherence of the cluster. For a bare site, $b = 1$, and when two sites j and k merge, the renormalized b-factor for the cluster C is:

$$b_C = b_j c_{DW,j} + b_k c_{DW,k} \qquad (42)$$

where $c_{DW,j}$ and $c_{DW,k}$ are the Debye-Waller factors (31). Hence, the total contribution of the cluster to the susceptibility, before the normalization by $\frac{1}{L^2}$, is:

$$\chi_C = \frac{b_C^2}{U_C} \qquad (43)$$

where b_C and U_C are the b-factor and charging energy of the cluster respectively. Further details of this calculation can be found in Appendix B.

For each lattice size, we obtain an estimate for the four quantities $s_{\max}$, s_2, $\Delta_{\min}$, and χ. Then, we examine how these estimates vary as we raise L. For certain types of distributions, computational limitations force us to work on relatively small lattices. This occurs, for example, when both $P_i(U)$ and $P_i(J)$ are bimodal, and we study this case in Figure 14.

In panel (a) of Figure 14, there is no cluster formation whatsoever. Hence, $s_{\max} = s_2 = 1$. This results in a gap $\Delta_{\min}$ that remains asymptotically constant as it cannot be lower than the lower bound of the initial charging energy distribution. The susceptibility χ also remains asymptotically constant.

Next, in panel (b), we find a regime in which link decimations do occur and clusters do form. Moreover, $s_{\max}$ and s_2 grow with system size, with what appears to be a power law for the largest lattice sizes that we explore. This growth is, however, subquadratic in L, meaning that $s_{\max}$ grows subextensively with lattice size. Meanwhile, $\Delta_{\min}$ decays with a power slower than L^{-2}, and the susceptibility χ remains constant with L.

In panel (c), all quantities show power law behavior out to $L = 100$, including the susceptibility which appears to grow with a very slow power. The growth of $s_{\max}$ is still slower than L^2, so the largest cluster is still subextensive.

Finally, in panel (d), we find a regime in which $s_{\max}$ grows as L^2, reflecting the formation of macroscopic clusters that scale extensively with the size of the lattice. The gap $\Delta_{\min}$ decays as L^{-2}, and the susceptibility shows an approximately L^4 growth for large L. Perhaps surprisingly, although s_2 grows with system size, it does so more slowly than it does in panel (c).
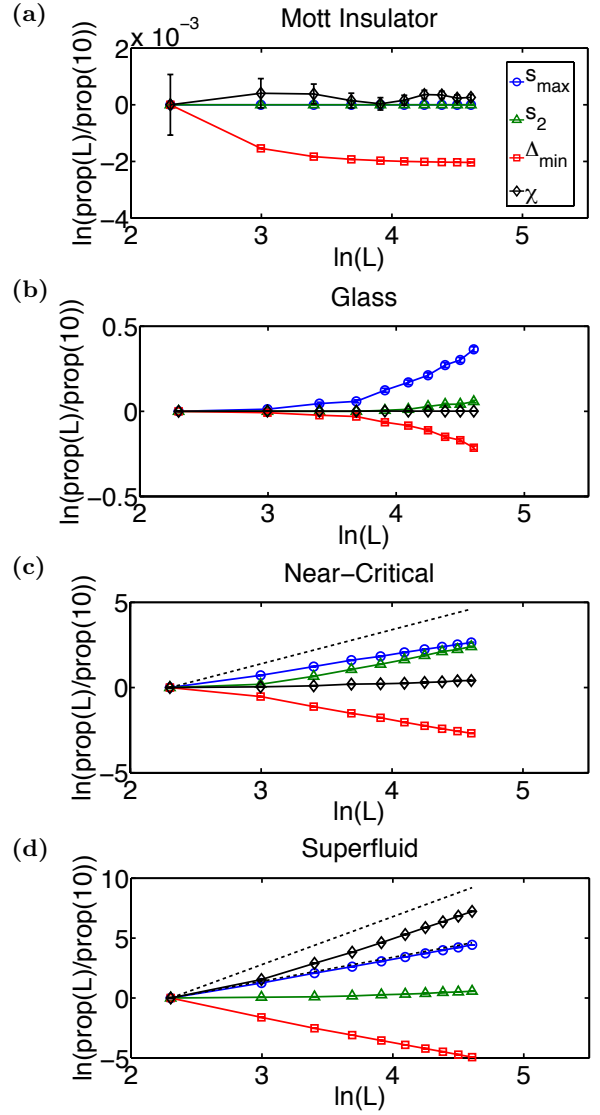

FIG. 14: Four characteristic behaviors of $s_{\max}$, s_2, $\Delta_{\min}$, and χ as a function of system size. Here, $P_i(U)$ and $P_i(J)$ are both bimodal, and J_h, the center of the higher peak of the Josephson coupling distribution, is used as the tuning parameter. All quantities have been normalized by their value for $L = 10$, and data is shown for $L = 10$ to $L = 100$. In panel (a), the quantities reflect the purely local physics of the Mott insulator. In panel (b), $s_{\max}$ and s_2 grow subextensively with system size, with what appears to be a power law. The gap also decays with a slow power, and the susceptibility remains constant. In panel (c), all quantities show power law behavior out to $L = 100$. The reference line shows L^2 growth. Panel (d) reflects the macroscopic clusters of the superfluid phase. The cluster size $s_{\max}$ is parallel to the L^2 reference line, and the susceptibility χ is parallel to the L^4 reference line for large L.

We now turn to a class of distributions for which we can reach larger lattice sizes. In particular, we return to the data set described in Appendix C, in which $P_i(U)$ is Gaussian and $P_i(J) \propto J^{-1.6}$. Data for this choice of

distributions is shown in Figure 15.

Panel (a) of this figure qualitatively reproduces the features of panel (a) of Figure 14. Panel (b) of the new figure, on the other hand, differs from panel (b) of Figure 14 in an important way. For large L, the power law behaviors of s_{max}, s_2 and Δ_{min} are lost, and all three quantities vary more slowly. In Figure 14, this effect may have been hidden by the use of smaller system sizes.

If the parameters are tuned such that the corresponding flow propagates very close to the unstable fixed point, then we *do* find a regime in which all quantities show nearly power law behavior out to $L = 300$. This regime is depicted in panel (c) of Figure 15.

Tuning past this point, we enter a regime in which macroscopic clusters form. Panel (d) of Figure 15 shows the behavior of the four quantities in this regime, and we see that most of the essential features of the corresponding panel of Figure 14 are reproduced. An important feature of the plot in panel (d) is that we can clearly see that the behavior of s_2 in this regime is closer to that observed in panel (b) than in the intervening panel (c).

The plots in Figures 14 and 15 are suggestively labeled with their corresponding phase identifications. We will provisionally use these labels for convenience in referring to these regimes, in advance of presenting arguments for these classifications in Section V. In the flow diagrams that we presented earlier, choices of initial distributions that correspond to the Mott insulating and glassy behaviors shown in panels (a) and (b) of Figures 14 and 15 flow to the stable insulating region where $\frac{\bar{J}}{U} \to 0$. The superfluid behavior in panel (d) of the figures corresponds to flows towards the high $\frac{\bar{J}}{U}$ regime of the flow diagrams. The pure power law behavior of panel (c) emerges for flows that propagate very close to the proposed unstable fixed point. This suggests that this fixed point may control the glass to superfluid transition of the disordered rotor model.

For now, we assume that this is the case and investigate more closely the behavior of physical quantities in the vicinity of this proposed transition. Having provided evidence of the universality that emerges near the critical point, here and in the remainder of this paper, we will focus exclusively on the choice of distributions detailed in Appendix C. In Figure 16, we show that plots of physical quantities vs. tuning parameter, taken for different L, can be collapsed onto universal curves. We will use this scaling collapse in Section V to determine the critical exponents governing the putative transition between glassy and superfluid phases.

D. Cluster Densities and b-factors

The physical property that distinguishes the Mott glass from the Bose glass is the compressibility. Later, we will show that, in order to calculate the compressibility, it is insufficient to consider just the minimum charging gap. Within each sample, the RG may form several clusters,
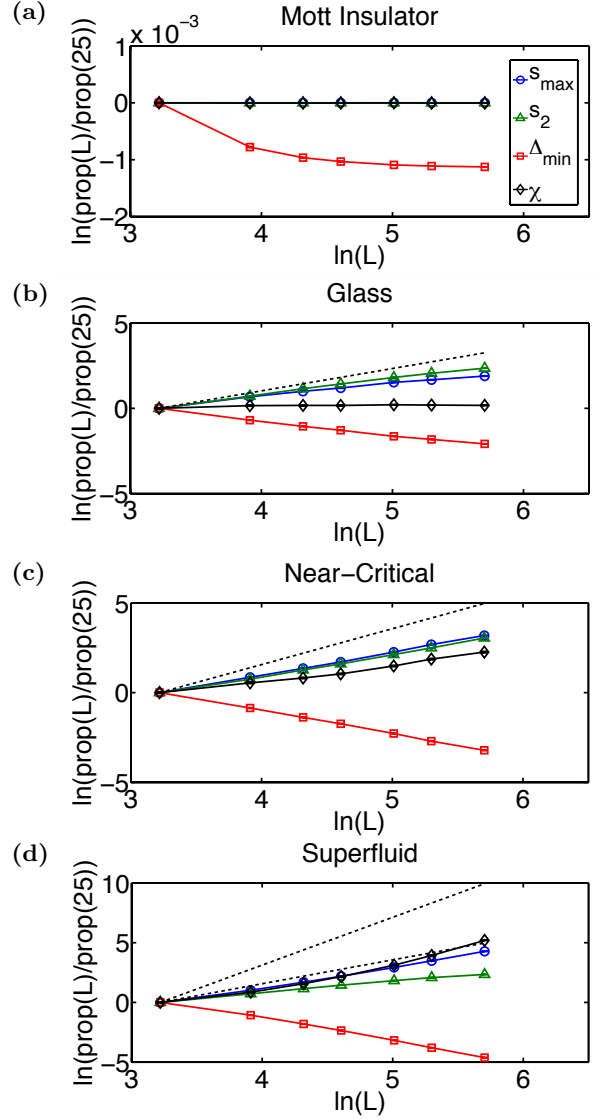

FIG. 15: Four characteristic behaviors of s_{max}, s_2, Δ_{min}, and χ as a function of system size. The initial distributions are those described in Appendix C. All quantities have been normalized by their value for $L = 25$, and data is shown for $L = 25$ to $L = 300$. In the four panels, $U_0 = 400$, 9.2, 8.97, and 8.8 respectively. Panel (a) reflects the purely local physics of the Mott insulator. Panel (b) shows a glassy regime characterized by rare-regions clusters that grow subextensively in system size. The reference line shows the power law that s_{max} obeys near criticality. This nearly critical regime is shown in in panel (c). The reference line here shows L^2 growth. Finally, panel (d) shows the superfluid regime, in which s_{max} is asymptotically parallel to the L^2 reference line. The susceptibility χ is expected to grow as L^4 for very large L, but it does not quite reach this behavior (indicated with a reference line) for $L \leq 300$.

each of which implies a local gap for adding and removing bosons. We will need to monitor all of these local gaps to find the compressibility.

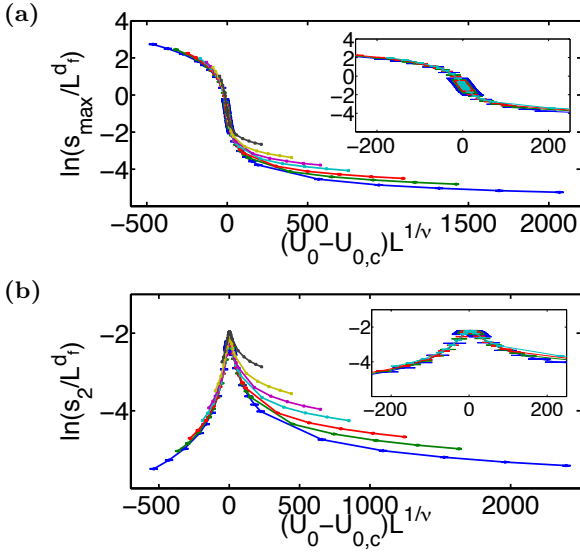More specifically, in this section, we will calculate the

(a)

(b)

FIG. 16: Panel (a) shows the scaling collapse of $s_{\max}$ as a function of tuning parameter, and panel (b) shows a similar collapse of s_2. Each line corresponds to a different value of the lattice size. We show data for $L = 25, 50, 75, 100, 150, 200,$ and 300. The insets show magnified views of the vicinity of the critical point for the four largest lattice sizes. The error bars, which are difficult to see in the larger plots, are clearly visible in the insets. To see the values of the exponents ν and d_f used in each panel, consult equations (71), (72), (76), and (77).

density (number per unit area) of clusters of a given size and of clusters with gaps in a given range of energy. We call these densities $\rho(s)$ and $\rho(\Delta)$ respectively. The latter quantity gives a "density-of-states" for addition of single bosons or holes to the system. For a single sample corresponding to a specific choice of initial distributions, we monitor the size and local charging gap for all the clusters formed during the renormalization, excluding bare sites that are not clustered by the RG. We pool data for 10^3 samples, choose a discretization of energy to determine a histogram bin size, compute a histogram of gaps and a histogram of cluster sizes, and finally normalize these histograms by the total simulated surface area: L^2 times the number of samples.

Our study of these densities will bring into focus the crucial difference between two types of clusters formed by the RG: rare-regions clusters and the macroscopic clusters that characterize the superfluid phase. We will, therefore, also take the opportunity to examine how the b-factors, which quantify the effect of harmonic fluctuations on the susceptibility, vary as a function of s for the two types of clusters.

The Charging Gap Density $\rho(\Delta)$

Note that $\rho(s)$ and $\rho(\Delta)$ are not particularly interesting for choices of distributions and parameters that
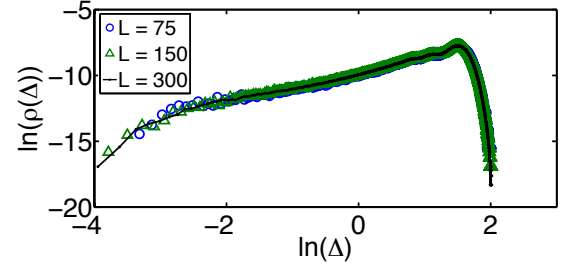

FIG. 17: The number per unity area of clusters with local gap near Δ for a choice of parameters in the glassy phase. The initial distributions are those described in Appendix C, with $P_i(U)$ Gaussian and $P_i(J) \propto J^{-1.6}$. The value of the tuning parameter is $U_0 = 8.8$, and this puts the system on the glassy side of the transition at $U_0 \approx 8.97$. Data is shown for $L = 75, 150,$ and 300 lattices. The density decays faster than a power law at small Δ.

yield the Mott insulating behavior from Figures 14 and 15. The profile of $\rho(\Delta)$ will be identical to the profile of the initial charging energy distribution, and because we choose this distribution to be bounded from below by some positive $U_{\min}$, it can be shown that this always corresponds to an incompressible phase. Hence, we begin by focusing on the glassy regime.

Figure 17 shows the gap density for a choice of parameters in the glassy phase. As the size of the lattice is raised, the density profile remains essentially invariant at large Δ, but smaller gaps, corresponding to larger clusters, begin to appear. However, these smaller gaps simply fill out a decay to 0 as $\Delta \to 0$.

Now, we turn our attention to the putative superfluid phase. The gap density in this phase is shown in Figure 18. In panel (a), there is an invariant piece to the distribution, but at very low Δ, a second peak appears as well. Panel (b) of Figure 18 shows a magnified view of this low Δ peak. This peak propagates towards $\Delta = 0$ as the system size is raised. Accompanying the propagation is a shrinking: the integrated weight of the low Δ peak shrinks as L^{-2}. The consequences of these two effects need to be taken into account carefully to calculate the compressibility.

The Cluster Size Density $\rho(s)$

We now consider how $\rho(s)$, the density of clusters of size s, varies as we sweep through the glassy regime and into the superfluid. Panel (a) of Figure 19 shows the approach to the transition from the glassy side. Very close to the transition at $U_0 \approx 8.97$, $\rho(s)$ exhibits a striking power law decay. Proceeding into the proposed glassy phase, the power law decay persists at small s. However, this behavior is cut off by some scale $\tilde{s}$, beyond which $\rho(s)$ decays very rapidly, essentially exponentially.

In panel (b), we proceed in the other direction from the putative transition, into the superfluid regime. A
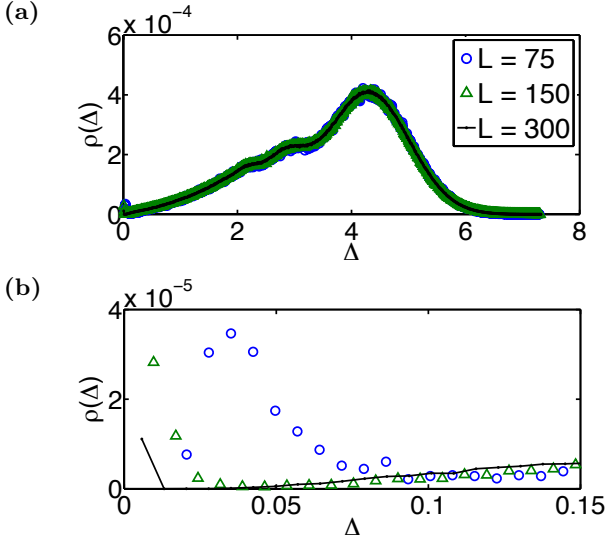
(a)

(b)

FIG. 18: In panel (a), the density (number per unit area) of clusters with a given gap Δ for a choice of parameters in the superfluid phase. The initial distributions are those described in Appendix C, with $P_i(U)$ Gaussian and $P_i(J) \propto J^{-1.6}$. The value of the tuning parameter is $U_0 = 9.2$, and this puts the system on the superfluid side of the transition at $U_0 \approx 8.97$. Data is shown for $L = 75$, 150, and 300 lattices. The density profiles exhibit two peaks. The broad peak that is visible in panel (a) remains invariant with L. To expose the second peak, we provide a magnified view of the low Δ part of the density in panel (b). This peak simultaneously shrinks and propagates towards $\Delta = 0$ as the system size is raised.
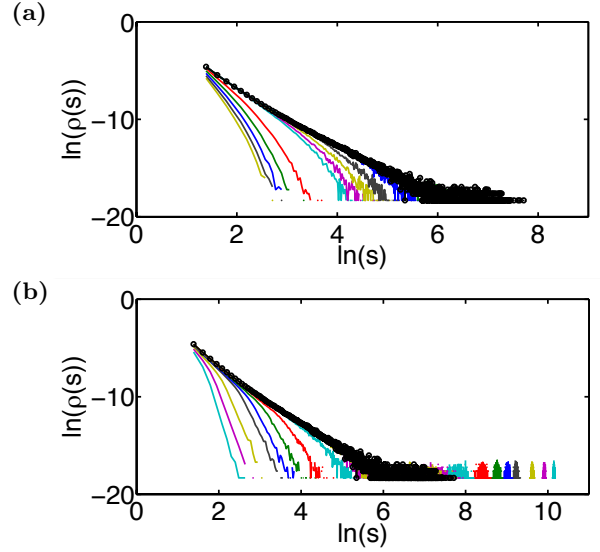
(a)

(b)

FIG. 19: Sweeps of $\rho(s)$ as the system is tuned through the superfluid-insulator transition. The initial distributions are those described in Appendix C, with $P_i(U)$ Gaussian and $P_i(J) \propto J^{-1.6}$. The tuning parameter is U_0, the center of $P_i(U)$. Panel (a) shows the sweep from deep in the glassy phase ($U_0 = 20$) to the transition ($U_0 = 8.97$). The closest data set to the transition is indicated by the black line with large data point markers. This line is reproduced in panel (b), which shows the sweep from the transition into the superfluid phase (up to $U_0 = 6.5$). In the superfluid phase, the density plot is characterized by a peak at large s and a remnant decay at low s.

peak, corresponding to the macroscopic clusters, appears at large s. The macroscopic cluster in each sample is dressed by rare-regions clusters, and these clusters are represented by the remnant decay at small s. While the large s peak is related to the low Δ peak in Figure 18, the remnant decay at small s is the analogue of the high Δ feature that stays invariant with system size. The low s decay in panel (b) of Figure 19 qualitatively resembles the decay well inside the glassy regime. In summary, $\rho(s)$ exhibits a pure power law decay in the vicinity of the proposed glass-superfluid transition; tuning away from criticality in either direction, and excluding the macroscopic clusters of the superfluid phase, the power law form of $\rho(s)$ only survives up to a scale $\tilde{s}$. For $s > \tilde{s}$, clusters become exponentially rare.

A type of scaling collapse can be performed for the $\rho(s)$ curves from Figure 19, and this collapse is shown in Figure 20. We will see below that this collapse gives a complementary set of critical exponents which are related by scaling to those that can be extracted from Figure 16.

Susceptibility b-factors

The data presented above for the cluster densities $\rho(s)$ and $\rho(\Delta)$ highlights the difference between the rare-
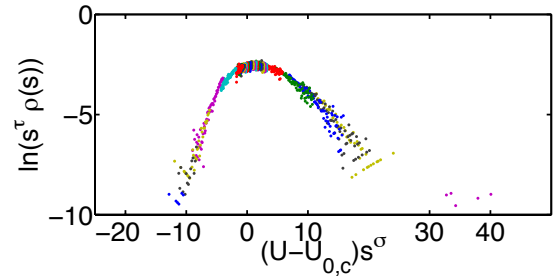

FIG. 20: Scaling collapse of the $\rho(s)$ curves from Figure 19. Small cluster sizes ($s < 30$) need to be discarded, because they are non-universal. Large cluster sizes ($s > 100$) need to be discarded, because they are noisy. Then, the remaining $\rho(s)$ curves, taken for different values of the tuning parameter, collapse onto a universal curve.

regions and macroscopic clusters generated by the RG. A
study of how the b-factors for the clusters vary as a func-
tion of s can bring out another difference between the
two types of clusters. Recall that the b-factor was intro-
duced in equation (43) to quantify the effect of harmonic
fluctuations on the susceptibility of a superfluid cluster.
As such, understanding the behavior of the b-factors will
also be essential in explaining the behavior of χ in the
various phases of our model.

In Figure 21, we plot the average value of b for a cluster
of size s and plot it against s. Again, we work with
$L = 300$ lattices and the choice of distributions described
in Appendix C. Panel (a) shows data for the glassy phase
and for the non-macroscopic clusters of the superfluid
phase. We see that $\bar{b}$ varies with s as a power law:

$$\bar{b}(s) \sim s^{\zeta} \tag{44}$$

and that the power is consistent for seven different choices
of the tuning parameter U_0. We will provide an estimate
of ζ in Section V. Panel (b) of Figure 21 shows data for
the macroscopic clusters when $U_0 = 8.8$. Now, $\bar{b}(s) \propto s$.
This behavior can be anticipated from a simple picture
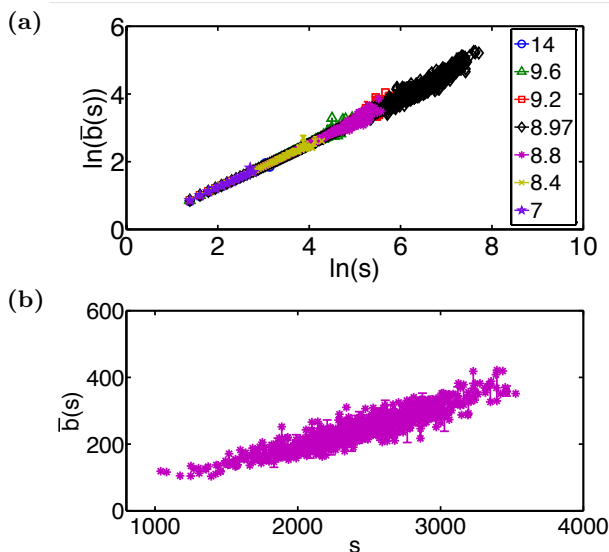of macroscopic cluster growth, which we will discuss in
Section V.

FIG. 21: The behavior of the mean b-factor for clusters of size
s as a function of s. In panel (a), we show data for the glassy
regime and for the non-macroscopic clusters of the superfluid
regime. The initial distributions are those described in Ap-
pendix C, and data is shown for seven values of the tuning
parameter U_0 on $L = 300$ lattices. The log-log plot shows
power law behavior of $\bar{b}(s)$ vs. s. In panel (b), we show data
for the macroscopic clusters when $U_0 = 8.8$. The plot indi-
cates that $\bar{b}(s) \sim s$ for macroscopic clusters. In both plots, the
error bars indicate the error on the mean $\bar{b}(s)$ over all clusters
of size s. For some of the largest and smallest values of s in
each plot, the absence of an error bar indicates that only one
cluster of that size was generated in all of the samples.

V. THE PHASES AND QUANTUM PHASE TRANSITIONS OF THE DISORDERED ROTOR MODEL

Having collected representative numerical data in the
previous section, we now assess what the data tells us
about the phases and phase transitions of our model. Our
first task will be to confirm the association of phases with
the behaviors of physical properties that we observed in
Figures 14 and 15. To this end, we will have to pre-
emptively introduce one of the main conclusions of the
discussion below: that our data points to a superfluid-
insulator transition driven by a percolation-type process.
The rare-regions clusters of the glassy phase find one an-
other, and their phases cohere, producing a macroscopic
cluster of superfluid ordering and driving the transition
to long range order and global superfluidity.

Motivated by this intuitive picture of the transition,
the logic of the discussion below will be the following:
in the proposed glassy and superfluid regimes of Figure
15, the cluster size density $\rho(s)$ exhibits the universal
features that we would expect from non-percolating and
percolating phases of standard models of percolation. We
can use these correspondences to extrapolate the behav-
iors seen in Figure 15 to the thermodynamic limit, in
the process showing that these phases will indeed have
the properties expected of glassy and superfluid phases.
Furthermore, we can analyze the critical point and ex-
tract the critical exponents that govern the superfluid-
insulator transition. After characterizing this transition,
we will finally return to the question of the identity of
the glassy phase and determine if a Mott glass is present
in the disordered rotor model (7).

Before proceeding, we should clarify that, although our
RG produces clusters with size distributions similar to
models of percolation, our transition is not the standard
percolation transition. Indeed, the exponents that we re-
cover are significantly different from the percolation ex-
ponents on a 2D square lattice. However, the analogy
to percolation allows us to easily identify the relations
between the various exponents and the scaling functions
for the observables.

A. Phases of the Model

Mott Insulator

We briefly digress to describe the phase of our model
in which the percolation picture is irrelevant, simply be-
cause there are no regions of superfluid ordering. In a
Mott insulating phase, the system wants to pin the num-
ber fluctuation to zero on each site to avoid the energetic
costs of charging. Hence, s_{max} and s_2 simply stay pinned
at one as L is raised. Meanwhile, Δ_{min} should asymptote
to a constant, reflecting the fact that the Mott insulator
is gapped. A phase without any cluster formation can be
described by completely local physics. This means that

the susceptibility can be approximated by disorder averaging a single site problem. In other words, χ should also stay constant as the system size is increased. Thus, in a Mott insulating phase, we expect exactly the behavior seen in panel (a) of Figures 14 and 15.

Glass

In non-percolating phases of standard models of percolation, the cluster size density is expected to go as:

$$\rho(s) = cs^{-\tau} f\left(\frac{s}{\tilde{s}}\right) \qquad (45)$$

where c is a constant. The function $f(x)$ is expected to be approximately constant for $x < 1$ and to rapidly decay for $x > 1$[28]. Equation (45) is consistent with what we have observed in our proposed glassy phase in panel (a) of Figure 19 and is also consistent with the expectation that, in a Griffiths phase, the frequency of occurrence of large rare-regions decays exponentially in their size[25]. In our numerics, $f(x)$ seems to follow a pure exponential decay $f(x) \sim e^{-x}$, but the conclusions we present below would be qualitatively unchanged if, for example, $f(x) \sim e^{-x^\lambda}$.

With the form of equation (45) in hand, we can now formulate a simple argument for the asymptotic behavior of $s_{\max}$. In particular, the order-of-magnitude of $s_{\max}$ is set by the condition[28]:

$$L^2 \sum_{s=s_{\max}}^{L^2} \rho_L(s) \approx 1 \qquad (46)$$

If the left hand side of equation (46) is less than 1, then it is unlikely that even one cluster of size greater than or equal to $s_{\max}$ will be present in a sample of size L^2. In equation (46), $\rho_L(s)$ is the finite size approximant to the function $\rho(s)$ that appears in equation (45). The upper limit of the sum in equation (46) is taken as L^2 because larger clusters simply cannot appear in the finite size sample. With enough sampling of the random distributions, it should, in principle, be able to accurately represent the approximant $\rho_L(s)$ out to $s = L^2$. The data indicates that $\rho_L(s)$ will simply reproduce $\rho(s)$ out to this value of s, so in the calculations below, we can replace the approximant $\rho_L(s)$ by $\rho(s)$. This will *not* be possible in the superfluid phase.

For large L, where we also expect $s_{\max} > \tilde{s}$, we can use equation (46) to find $s_{\max}$ by computing

$$
\begin{aligned}
L^2 \sum_{s=s_{\max}}^{L^2} \rho(s) &\approx L^2 \int_{s_{\max}}^{L^2} ds\, \rho(s) \\
&= cL^2 \int_{s_{\max}}^{L^2} ds \exp\left[-\frac{s}{\tilde{s}} - \tau \ln(s)\right] \\
&\approx cL^2 \int_{s_{\max}}^{L^2} ds \exp\left[-\frac{s}{\tilde{s}}\right] \\
&= c\tilde{s}L^2 \left(e^{-\frac{s_{\max}}{\tilde{s}}} - e^{-\frac{L^2}{\tilde{s}}}\right) \qquad (47)
\end{aligned}
$$

Setting this expression equal to 1 and inverting for $s_{\max}$, we find that, asymptotically in L:

$$s_{\max} \sim \ln L \qquad (48)$$

For large clusters, the link decimation rule for addition of charging energies (26) implies that $U \sim s^{-1}$, and therefore:

$$\Delta_{\min} \sim \frac{1}{\ln L} \qquad (49)$$

An entirely analogous condition to equation (46) can be formulated for s_2. We simply replace the right hand side of equation (46) with two, indicating that we want to find the value of s such that there are likely to be two clusters of that size or greater in a typical sample. However, the remainder of the calculation is qualitatively unaffected by this change. Therefore, s_2 should also grow logarithmically in this regime:

$$s_2 \sim \ln L \qquad (50)$$

Finally, we turn to the susceptibility. This can be computed as follows:

$$
\begin{aligned}
\chi &= \frac{1}{L^2} \sum_C \frac{b_C^2}{U_C} \\
&\sim \frac{1}{L^2} \sum_C s_C b_C^2 \\
&\sim \frac{1}{L^2} \sum_{s=1}^{s_{\max}} \rho(s) L^2 (\bar{b}(s))^2 s \\
&= \sum_{s=1}^{s_{\max}} \rho(s) (\bar{b}(s))^2 s \qquad (51)
\end{aligned}
$$

In this calculation, the sum over C is a sum over clusters, with s_C being the size of the cluster. Then, the sum over s is, as before, a sum over cluster sizes, and $\bar{b}(s)$ is the average value of the b-factor for a cluster of size s. Figure 21 shows that, in the glassy regime, $\bar{b}$ varies as a power of s and that this power remains the same all the way up to criticality. While we do not have a complete understanding of this behavior, we can still understand the asymptotic behavior of χ by reasoning that $\bar{b}$ can, at most, grow linearly in s. This follows from an interpretation of the b-factor as the effective number of rotors that order with the field in a cluster of size s. Since $\rho(s)$ decays exponentially for large s while $\bar{b}(s)$ grows at most as a power, the sum (51) converges, and χ should be asymptotically constant:

$$\lim_{L\to\infty} \chi = \chi_\infty \qquad (52)$$

All of these behaviors are consistent with what has been observed numerically in panel (b) of Figure 15. Moreover, since logarithmic behavior can be difficult to discriminate from a slow power law at low L, they are

also consistent with panel (b) of Figure 14. Thus, under the numerically justified assumption that this regime corresponds to a non-percolating phase, we can deduce that, as L increases, arbitrarily large rare-regions of superfluid ordering will appear, driving the gap to zero. However, the typical size of these regions grows extremely slowly (i.e. logarithmically) with system size. The fraction of sites occupied by the largest cluster in a typical sample vanishes as $L \to \infty$, so there is no long range order. The behavior of this phase for large L corresponds to what we should expect for a glassy phase.

Critical Region

At the critical point of a percolation transition, the cluster size scale in equation (45) is expected to diverge as:

$$\tilde{s} \sim |g - g_c|^{-\frac{1}{\sigma}} \tag{53}$$

where g is the tuning parameter for the transition. This divergence is related to the divergence of a correlation length which indicates the typical linear extent of the largest clusters:

$$\xi \sim |g - g_c|^{-\nu} \tag{54}$$

By equation (53), $\rho(s)$ is a power law at criticality:

$$\rho(s) = c s^{-\tau} \tag{55}$$

This means that the critical point is characterized by a scale invariant, fractal structure of clusters[28]. In turn, this implies that ξ and $\tilde{s}$ are related by a fractal dimension:

$$\tilde{s} = \xi^{d_f} \tag{56}$$

Equations (53), (54), and (56) together imply:

$$\sigma = \frac{1}{\nu d_f} \tag{57}$$

We will use this scaling law in our analysis of the transition below[28].

For the present purposes, note that equation (55) is once again consistent with what we have observed numerically in Figure 19. Now, the calculation for $s_{\max}$ becomes:

$$L^2 \sum_{s=s_{\max}}^{L^2} \rho(s) \approx c L^2 \int_{s_{\max}}^{L^2} ds\, s^{-\tau} = 1 \tag{58}$$

which, when inverted, yields:

$$
\begin{aligned}
\ln s_{\max} \;=\; & \frac{2}{\tau - 1} \ln L - \frac{1}{\tau - 1} \ln\left(\frac{\tau - 1}{c}\right) \\
& + \ln\left(1 + \frac{c}{(\tau - 1)L^{2(\tau - 2)}}\right)
\end{aligned} \tag{59}
$$

Asymptotically, as long as $\tau > 2$, this simply corresponds to a power law growth of $s_{\max}$:

$$s_{\max} \sim L^{\frac{2}{\tau - 1}} \tag{60}$$

On the other hand, since d_f is the exponent that connects length and cluster size scales at the transition, equation (60) yields another scaling relation:

$$d_f = \frac{2}{\tau - 1} \tag{61}$$

Equations (57) and (61) are the usual scaling laws connecting exponents at a percolation transiiton[28].

In accordance with equation 60, the gap should close as:

$$\Delta_{\min} \sim L^{-\frac{2}{\tau - 1}} = L^{-d_f} \tag{62}$$

Furthermore, as in the glassy regime, the qualitative behavior of the second largest cluster size s_2 should be identical to that of $s_{\max}$:

$$s_2 \sim L^{\frac{2}{\tau - 1}} \tag{63}$$

Turning to the susceptibility, we find that it no longer converges to a finite value. At criticality, power law behavior of $\bar{b}(s)$ follows naturally from scale invariance. When $\rho(s) \sim s^{-\tau}$ and $\bar{b}(s) \sim s^{\zeta}$:

$$
\begin{aligned}
\chi \;=\; & \sum_{s=1}^{s_{\max}} \rho(s)(\bar{b}(s))^2 s \\
\sim\; & \int_1^{s_{\max}} ds\, s^{1 + 2\zeta - \tau} \\
\sim\; & s_{\max}^{2 + 2\zeta - \tau} \\
\sim\; & L^{\frac{4 + 4\zeta - 2\tau}{\tau - 1}} \\
=\; & L^{d_f(1 + 2\zeta) - 2}
\end{aligned} \tag{64}
$$

From Figure 21, we can estimate the exponent ζ:

$$\zeta \approx 0.68 \pm 0.01 \tag{65}$$

With another choice of initial distributions ($P_i(U)$ bimodal and $P_i(J) \propto J^{-1.6}$), we have found a similar value for ζ. If $d_f(1 + 2\zeta) > 2$, then χ asymptotically diverges as a power law, as seen in Figure 15. We will provide an estimate of d_f shortly in equation (72). For now, we note that the power observed for χ vs. L in Figure 15 is consistent with this estimate of d_f and the estimate for ζ that is given above. In Figure 14, the relatively small system sizes likely put us out of the scaling regime for χ, and this is probably responsible for the extremely slow growth of χ with L.

Superfluid

The percolating phase is characterized by the presence of a macroscopic cluster that grows with the size of the lattice, so trivially:

$$s_{\max} \propto L^2 \tag{66}$$

and therefore:

$$\Delta_{\min} \propto L^{-2} \qquad (67)$$

It is possible to construct an argument along the lines of condition (46) for the behavior of $s_{\max}$ in equation (66), but in this case, it is important *not* to substitute the infinite lattice density $\rho(s)$ for the finite size approximant $\rho_L(s)$. The subtlety lies in the high s peak observed in the density plots in panel (b) of Figure 19. Consistent with their low Δ counterparts in the plots of the gap density, the location of these peaks propagates as L^2 towards high s as L is raised. Simultaneously, the integrated weight of the peaks shrinks as L^{-2}, reflecting the fact that there is only one macroscopic cluster in each sample. Balancing the shrinking and propagation, it is possible to see that, in order to achieve the condition (46), $s_{\max}$ must scale as shown above in equation (66).

The reasoning above has important implications for the behavior of s_2. Since the weight of the high s peak of $\rho_L(s)$ shrinks as L^{-2}, the second largest cluster must be drawn from the remnant low s decay. The physical picture behind this low s decay is the following: suppose we remove the sites belonging to the macroscopic cluster from the original lattice. In doing so, we remove some of the lowest charging energies and highest Josephson couplings from the bare lattice. Consequently, the remnant lattice is globally insulating. Nevertheless, rare-regions of superfluid ordering can form exactly as in the glassy phase. It follows that s_2 will grow with L as in the glassy phase:

$$s_2 \sim \ln L \qquad (68)$$

This is responsible for the peak in s_2 at criticality.

To calculate the susceptibility, we first take into account the contribution of the macroscopic cluster. The behavior of $\bar{b}(s)$ for a macroscopic cluster can be inferred from a simplified picture of a large cluster merging with single neighbors. As the macroscopic cluster grows, its charging energy becomes smaller, driving the Debye-Waller factor for the cluster to one. At the same time, the cluster's Josephson couplings to other sites grow through link addition processes. This means that the Debye-Waller factor for another site that is merging with the macroscopic cluster also approaches unity. Therefore, the b-factor addition rule (42) approximately becomes $\tilde{b}_C = b_C + 1$, and $b_C \sim s_C$ follows. Then:

$$
\begin{aligned}
\chi_{mac} &= \frac{1}{L^2} \times \frac{(\bar{b}(s_{\max}))^2}{\Delta_{\min}} \\
&\sim \frac{1}{L^2} \times \frac{s_{\max}^2}{\Delta_{\min}} \\
&\sim L^4 \qquad (69)
\end{aligned}
$$

The rare-regions clusters dressing the macroscopic cluster add a subleading contribution to the susceptibility, which we call χ_{rr}. The reasoning of equation (52) indicates that this contribution should be asymptotically constant.

	Mott Insulator	Glass	Critical	Superfluid
$s_{\max}$	const.	$\ln(L)$	L^{d_f}	L^2
s_2	const.	$\ln(L)$	L^{d_f}	$\ln(L)$
$\Delta_{\min}$	const.	$\frac{1}{\ln(L)}$	L^{-d_f}	L^{-2}
χ	const.	const.	$L^{d_f(1+2\zeta)-2}$	L^4

TABLE I: Large lattice size (L) behavior of physical properties in the three phases and at the critical point of the glass-superfluid transition. Note that our estimate of d_f from data for s_2, given in equation (77), differs quantitatively from our estimate from s_{max}, given in equation (72). We suspect that the estimate from the s_2 data is influenced by finite size effects, and we therefore take the estimate (72) to be our best approximation to d_f.

Thus, the quartic behavior of equation (69) is the correct asymptotic behavior. Finite size corrections from χ_{rr} will modify this behavior, however, and this is probably why we do not quite see χ reach the L^4 behavior in panel (d) of Figure 15.

We have now provided arguments for the behaviors observed in each panel of that figure, and we summarize this information in Table I.

B. Quantum Phase Transitons

Glass-Superfluid Transition

Earlier, we remarked in passing that systems exhibiting the behaviors that we have now identified as Mott insulating and glassy eventually propagate towards the putative insulating region to the top left of the numerical flow diagrams. Correspondingly, the systems exhibiting superfluid behavior propagate towards the putative superfluid region to the bottom right. We can now verify our tentative identifications of these stable regions of the diagram. We can also determine that the unstable fixed point controls the transition between the glass and the superfluid, the superfluid-insulator transition of our disordered rotor model. This allows us to draw the schematic picture of the flow diagram that we presented in Figure 1.

We will now focus on the critical region and extract critical exponents governing the glass-superfluid transition. Estimating these exponents requires formulating scaling hypotheses for the behavior of physical quantities in the critical region. In the case of $s_{\max}$[28]:

$$s_{\max} = L^{d_f} h_1 \left(\frac{L}{\xi} \right) = L^{d_f} \tilde{h}_1(L^{\frac{1}{\nu}}(g - g_c)) \qquad (70)$$

Exactly at criticality, $s_{\max} \sim L^{d_f}$ asymptotically, so plotting $\frac{s_{\max}}{L^{d_f}}$ vs. $(g-g_c)$ generates a crossing of the curves for different lattice sizes. Slightly away from criticality, the power law behavior should persist if $L < \xi$. For $L > \xi$, the system recognizes that it is not critical and we should

see a crossover to logarithmic growth on the glassy side and L^2 growth on the superfluid side. Hence, $\frac{L}{\xi}$ is the important ratio near criticality, and this motivates scaling form (70). The scaling form, in turn, implies that we can produce scaling collapse by plotting $\frac{s_{\max}}{L^{d_f}}$ vs. $(g - g_c)L^{\frac{1}{\nu}}$. This is what we have done in panel (a) of Figure 16. This scaling collapse leads to the estimates:

$$\nu \approx 1.09 \pm 0.04 \qquad (71)$$

$$d_f \approx 1.3 \pm 0.2 \qquad (72)$$

These estimates and error bars are obtained through the following procedure: first, to find an estimate of the critical value of the tuning parameter g, we examine the behavior of the sample average of s_2 vs. g. Since s_2 varies as a power law in L exactly at criticality and grows more slowly within the phases, s_2 should exhibit a maximum at g_c. We can find the error Δg_c on our estimate of g_c by taking the window of values of g around g_c for which the sample average of s_2 is within one error bar of the maximum. To proceed to obtain estimates for ν and d_f, we now partition our data into bins of size N_b samples. For example, the first bin may consist of the first $N_b = 50$ samples for each value of the tuning parameter and each lattice size L. Our immediate goal is to find the best values of ν and d_f for this subset of our data. We first focus on the data for $g = g_c$ and do linear regression to find the best exponent that describes the power law growth of the average value of $s_{\max}$ with L. This gives an estimate of d_f for the bin. Next, for two lattice sizes (typically, $L = 150$ and $L = 300$), we compute an average of $s_{\max}$ over the samples in the bin for several values of the tuning parameter around g_c. Then, using the previous estimate of d_f for the bin and the scaling hypothesis (70), we test various values of ν until we achieve the best collapse. Thus, we also obtain an estimate of ν for the bin. From the distribution of estimates for the different bins, we can find mean values and error bars for d_f and ν. However, these error bars do not take into account the error on our estimate of the critical point. To propagate this error, we need to repeat the critical point estimation procedure using $g_c + \Delta g_c$ and $g_c - \Delta g_c$ as our estimates of the critical point. We thank Bryan Clark for outlining the general strategy of putting error bars on our exponents and a referee for helpful comments on sources of error to incorporate into our estimates.

We have repeated the scaling collapse of $s_{\max}$ for a different choice of initial distributions: bimodal $P_i(U)$ and $P_i(J) \propto J^{-1.6}$. For these distributions, we have used a different choices of the two lattice sizes that we consider when searching for an estimate of ν ($L = 100$ and $L = 200$). Ultimately, we have been able to recover estimates for ν and d_f which are consistent with (71) and (72):

$$\nu \approx 1.1 \pm 0.1 \qquad (73)$$

$$d_f \approx 1.2 \pm 0.2 \qquad (74)$$

A completely analogous scaling hypothesis can be made for s_2:

$$s_2 = L^{d_f} h_2\left(\frac{L}{\xi}\right) = L^{d_f} \tilde{h}_2(L^{\frac{1}{\nu}}(g - g_c)) \qquad (75)$$

Then, the exponents needed to produce the collapse in panel (c) of Figure 16 are:

$$\nu \approx 1.06 \pm 0.09 \qquad (76)$$

$$d_f \approx 1.31 \pm 0.07 \qquad (77)$$

Since all the estimates (71)-(77) are consistent, we will proceed using our tightest estimates on these exponents: (71) and (77).

We now note that a scaling hypothesis can also be formulated for the density $\rho(s)$. From equation (45), we see that, for fixed lattice size L, $s^\tau \rho(s)$ should depend only on the combination $\frac{s}{\bar{s}} \sim s(g - g_c)^{\frac{1}{\sigma}}$. Hence, by plotting $s^\tau \rho(s)$ vs. $s(g - g_c)^{\frac{1}{\sigma}}$ and tuning until the curves for different choices of g collapse, we ought to be able to extract estimates for τ and σ. On the other hand, τ and σ are related to ν and d_f through the scaling relations (61) and (57), so from the estimates (71) and (77), we can infer:

$$\tau \approx 2.53 \pm 0.08 \qquad (78)$$

$$\sigma \approx 0.70 \pm 0.04 \qquad (79)$$

In Figure 20, we attempt to produce collapse of $\rho(s)$ for $L = 300$ lattices using these estimates of τ and σ. To produce this plot, we need to discard data points for small cluster sizes ($s < 30$), because they are non-universal, and for large cluster sizes ($s > 100$), because they are noisy. Once we do this, the collapse works fairly well, indicating that we have found a consistent set of critical exponents obeying the necessary scaling relations.

Comments on the Insulator-Insulator Transition

Before proceeding further, we should note that our numerics do not accurately capture the boundary between the Mott insulator and the Mott glass. Several authors have argued that we should expect glassy behavior to occur whenever the ratio of the largest bare Josephson coupling to the lowest bare charging energy $\frac{J_{\max}}{U_{\min}}$ exceeds the value of the clean transition, because this condition allows for the presence of regions in which the system locally looks like it is in the superfluid phase[6,15]. However, in the strong disorder RG treatment, some distributions that satisfy this criterion still produce Mott insulating behavior out to the largest lattice sizes that we investigate. Since the glassy phase occurs due to rare-regions or Griffiths effects, a finite size system will only look glassy if it is large enough for the rare-regions to

appear. This suggests that some choices of parameters which yield Mott insulating behavior on finite size lattices may actually yield glassy behavior in the thermodynamic limit. Of course, this difficulty necessarily afflicts all numerical methods (except those that rely on mean-field type approximations[29]), since they are confined to operate on finite size systems.

We will not comment on this transition further, but we take this opportunity to refer the reader to papers by Krüger et al. and Pollet et al., which present two viewpoints on the Mott insulator to Bose glass transition[6,30].

C. Identifying the Glass

Finally, we return to the question of the identity of the glassy phase. Is the phase a Bose glass or a Mott glass? A definitive diagnosis requires a measurement of the compressibility:

$$\kappa = \frac{1}{L^2} \sum_j \frac{\partial \langle \hat{n}_j \rangle}{\partial \mu} \bigg|_{\mu=0} \tag{80}$$

The compressibility is more subtle to measure than the quantities that we have already discussed. Any finite size system is gapped and therefore incompressible. On the other hand, in the thermodynamic limit, the gap can vanish and the compressibility need not be zero.

How can we measure the compressibility of the glassy phase in the RG? In Figures 17 and 18, we presented data for the density (number per unit area) of clusters with a given gap Δ. With this density profile in hand, we can calculate the density of particles introduced to the system by a small chemical potential shift μ:

$$\begin{aligned} \rho_{\text{ex}} &= \int_0^\mu d\Delta \rho(\Delta) n(\Delta) \\ &= \int_0^\mu d\Delta \rho(\Delta) \lfloor \frac{\mu}{2\Delta} - \frac{1}{2} \rfloor \\ &\approx \int_0^\mu d\Delta \rho(\Delta) \left(\frac{\mu}{2\Delta} - \frac{1}{2} \right) \end{aligned} \tag{81}$$

Here, $n(\Delta)$ is the number of particles added to a cluster with gap Δ if the chemical potential is μ. If $\rho(\Delta)$ stays finite as $\Delta \to 0$, the integral is divergent, and the system is infinitely compressible. Suppose alternatively that $\rho(\Delta)$ vanishes as Δ^β for small Δ. Then:

$$\int_0^\mu d\Delta \Delta^\beta \left(\frac{\mu}{2\Delta} - \frac{1}{2} \right) = \frac{\mu^{\beta+1}}{2\beta(\beta+1)} \tag{82}$$

The derivative of the integral vanishes at $\mu = 0$ for $\beta > 0$. Thus, the system is incompressible. Comparing to the data shown in Figures 17, we see that there is no numerical evidence for a finite glass compressibility; the gap density appears to vanish even faster than a power law as $\Delta \to 0$. This is consistent with the behavior of $\rho(s)$ in equation (45), since Δ is expected to scale as s^{-1}.

Hence, the numerics imply that the Mott glass intervenes between the Mott insulator and the superfluid in this model.

At first glance, the preceding argument may be troubling. Due to the shrinking of the low Δ peak in panel (b) of Figure 18, the gap density $\rho(\Delta)$ also appears to vanish as $\Delta \to 0$ in the superfluid phase. The caveat is that it is necessary to more carefully evaluate the competing effects of the shrinking and the propagation. The low Δ peak in Figure 18 represents the macroscopic superfluid clusters that form in the superfluid phase. These clusters do not appear in proportion to the surface area of the sample, as is the case for rare-regions clusters; instead, one such macroscopic cluster appears in each sample. Therefore, the density of macroscopic clusters will go as $\frac{1}{L^2}$, and this is responsible for the shrinking of the low Δ peak. The propagation of the peak, meanwhile, reflects the fact that the gap closes as L^{-2}. For a fixed choice of μ, the number of bosons that will be added to these macroscopic clusters scales as:

$$\frac{\mu}{2\Delta} - \frac{1}{2} \propto \mu L^2 \tag{83}$$

for large L. Then, the *density* of particles introduced to the system is:

$$\rho_{\text{ex}} \propto \frac{1}{L^2} \times \mu L^2 = \mu \tag{84}$$

This directly implies that the compressibility (80) is a constant in the thermodynamic limit, so we recover the expected result that the superfluid phase is compressible.

VI. CONCLUSION

While the interplay of disorder and interactions in bosonic systems has attracted considerable interest for nearly three decades, the random boson problem remains a fertile source of intriguing physics. In this paper, we have investigated a particular model of disordered bosons, the two-dimensional rotor (or Josephson junction) model. Our strong disorder RG analysis suggests the presence of an unstable finite disorder fixed point of the RG flow, near which the coupling distributions flow to universal forms. Furthermore, the strong disorder renormalization procedure indicates the presence of three phases of the model: the Mott insulating and superfluid phases of the clean model are separated in the phase diagram by an intervening glassy phase. The unstable fixed point governs the transition between the superfluid and this glassy phase, and the transition is driven by a kind of percolation. The RG procedure also provides evidence that this glassy phase is, in fact, the incompressible Mott glass.

Our work is a numerical extension into two dimensions of the one-dimensional study by Altman, Kafri, Polkovnikov, and Refael[13]. The 2D fixed point, however, differs from the 1D fixed point in an important

way. The 1D fixed point occurs at *vanishing* interaction strength (all charging energies $U_j = 0$). Thus, it corresponds to a completely classical model and reveals that the superfluid-insulator transition can be tuned by varying the width of the Josephson coupling distribution at arbitrarily small interaction strength. The 2D fixed point is, in contrast, fully quantum. Indeed, in the critical distributions generated by the strong disorder RG, the charging energy distribution is peaked near the RG scale while the Josephson coupling distribution is peaked well below.

On the other hand, the fixed point that we have identified in this paper is similar to its 1D counterpart in that it does not exhibit infinite randomness. Finite disorder fixed points are not optimal settings for strong disorder renormalization analyses, because the procedure does not become asymptotically exact near criticality and is, in this sense, an uncontrolled approximation. We have proceeded with such an analysis anyway. In doing so, we have found a robust fixed point controlling the superfluid-insulator transition and phases exhibiting reasonable physical properties. While this may be surprising given the perils of the method, we have attempted to argue for the appropriateness of the method, as an *approximation*, through an analysis of the RG steps in light of the forms of the fixed point distributions $P_{\text{univ}}(U)$ and $P_{\text{univ}}(J)$. We certainly acknowledge that there are other subtleties due to the lack of infinite randomness; for example, the notion of a superfluid cluster is not completely sharp, and consequently, percolation of superfluid clusters can only be an approximate picture of the transition[31]. Nevertheless, the structure of the fixed point Josephson distribution (36) suggests that the picture may be a good approximation, and we take this opportunity to remind the reader that we extensively discuss the reliability of the RG, in light of the properties of the fixed point, in Appendix D. Moreover, the self-consistency of our numerical results, especially the striking universality and robustness of the unstable fixed point, gives us confidence that our strong disorder RG analysis provides useful information about the system. With the potential caveats in mind, we therefore turn to exploring connections with other theoretical, numerical, and experimental work.

The Mott glass phase of the two-dimensional model is the straightforward analogue of the phase found in one dimension by Altman et al. The charging gap, the energy needed to add or remove a boson from the system, vanishes due to the presence of arbitrarily large rare-regions of superfluid ordering. However, there is no true long range order because these rare-regions grow subextensively with system size. If a small chemical potential shift is turned on, it becomes energetically preferable to add bosons somewhere in the system, specifically in the largest of the rare-region superfluid clusters. Nevertheless, these clusters do not occur with sufficient number to produce a finite density of bosons, and the glass remains incompressible. In a Monte Carlo study of a model similar to ours, Prokof'ev and Svistunov previously found evidence for a glassy phase in which the compressibility vanishes for this reason[32]. Moreover, the Mott glass that was identified by Roscilde and Haas in a related spin-one model also relies on the same mechanism[33]. The original proposal of Giamarchi, Le Doussal, and Orignac is, however, fundamentally distinct[12]. In their Mott glass, the charging gap remains finite, guaranteeing a vanishing of the compressibility; however, gaplessness is achieved through the closing of a mobility gap for transport of particles between nearby insulating and superfluid patches. Sengupta and Haas have argued that particle-hole symmetry, a crucial ingredient in the formation of our Mott glass, is not necessary for the realization of the phase through this alternative mechanism[34].

In the superfluid phase, true long range order emerges because the largest cluster scales with the size of the lattice. In this sense, this cluster is macroscopic. Despite this, near the transition, the macroscopic cluster may only occupy a small fraction of the total number of lattice sites. Because the clustering procedure can merge sites that are not nearest neighbors in the bare lattice, the fraction of insulating sites may actually exceed the standard 2D square lattice percolation threshold. Even with such a large fraction of insulating sites, a superfluid phase can still exist because virtual tunneling processes can carry supercurrent through the insulating sites, allowing for macroscopic superfluidity on the "depleted" lattice that forms when the insulating sites are removed from the lattice by site decimation.

Nevertheless, the Mott glass to superfluid transition of our model should be contrasted with transitions that arise when disorder is introduced to a 2D square lattice by bond or site depletion[33,35–39]. Models of the latter type only have the opportunity to form long range ordered phases when the underlying lattice is percolating. This percolation is purely classical and exhibits all the critical properties expected of standard site or bond percolation on a square lattice[28]. The superfluid-insulator transition is, in general, distinct from this transition; once the underlying lattice percolates, the bosonic model defined on that lattice may still exhibit Mott insulating, glassy, and superfluid phases[33]. In contrast, the only percolation-type process in our model is the one that actually drives the superfluid-insulator transition. The critical properties of this transition differ dramatically from those of classical 2D square lattice percolation, because the transition is not a purely geometric phenomenon. Instead, there are quantum tunneling processes overlaid on top of a geometric structure[40].

We have remarked that several experimental groups are currently working on studying disordered bosonic systems in ultracold atoms[8–11]. Dirty and granular superconductors provide another experimental context that may be relevant to the physics of this paper. The question of the applicability of bosonic pictures to the 2D superconductor-insulator quantum phase transition is long-standing. Recently, this problem has been ad-

dressed numerically by Bouadim et al., who used quantum Monte Carlo simulations to study a fermionic model of the transition and found that bosonic physics emerges at criticality[41]. This issue has also been addressed experimentally by Crane et al. These authors studied indium oxide thin films and measured a superfluid stiffness in the insulating state, indicating that Cooper pairs may survive into the insulating region[42]. This leaves open the possibility that the transition is driven by percolation of superconducting regions, a possibility that has also been explored in experiments on granular superconductors by Frydman et al. and Sherman et al. [43,44]. During the preparation of this manuscript, we learned of a recent experiment by Allain et al. on tin-decorated graphene. Intriguingly, this experiment may point to a superconductor-insulator transition that is bosonic in nature, driven by percolation, and characterized by critical exponents similar to those identified by our work[45].

Motivated by the link between the Mott glass and particle-hole symmetry, Roscilde and Haas have proposed a different class of experimental systems in which Mott glass physics may be present: nickel based spin-one antiferromagnets. The advantage in these spin systems is that it may be easier to realize particle-hole symmetry in the guise of Z_2 symmetry[33]. Very recently, Yu et al. have followed up on this proposal with an experimental investigation of Bose and Mott glass phases in bromine-doped dichloro-tetrakis-thiourea-nickel[46]. This system is three-dimensional, so the character of the transition would naturally differ from what we have calculated in this paper.

One immediate extension of our study would be to consider adding random filling offsets to the disordered rotor model, as Altman et al. did in a follow-up to their work on the 1D model[14]. The intuition from 1D suggests that such a model would contain a Bose glass phase. On the other hand, very recent Monte Carlo work by Wang et al. indicates that the Mott glass survives the substitution of exact particle-hole symmetry with *statistical* particle-hole symmetry[47]. In one dimension, Altman et al. found that the universality class of the transition (but not the identity of the glassy phase) is independent of the symmetry properties of the random filling offsets, but the situation may differ in $d > 1$; this remains to be understood.

Another interesting extension may be to study the rotor model defined on random networks. Suppose we do not begin with a square lattice but rather with a generalized network of mean connectivity $z = 4$. At its critical point, would such a model flow to the same fixed point as the model defined on a square lattice? The fact that the strong disorder RG modifies the initial lattice structure into a more general network suggests that this may be the case for at least some types of random networks. Next, suppose we vary the mean connectivity from $z = 4$. Is there a range of connectivities for which random network models access our fixed point?

Perhaps it would be better to precede such investigations with a better characterization of the fixed point itself. In one dimension, Altman et al. were able to write down master equations for the RG flow, solve them to find fixed point distributions, and then verify numerically that these distributions are stable[13]. In two dimensions, a direct analytical approach is more difficult, and it remains to be seen whether such an approach is tractable. Our work provides suggestive numerical evidence regarding the forms of the universal distributions that characterize the critical point of the disordered rotor model (7). A Lyapunov analysis of these distributions, in which the RG is used as a tool to identify irrelevant directions in the space of possible distributions, could be a useful step in clarifying the critical forms still further. Then, analytically *verifying* these forms as attractor solutions of the RG flow may be an easier task than analytically identifying them would have been in the absence of any numerical guidance.

Recent work by Vosk and Altman suggests yet another direction for connecting the results of the RG to experiment. These authors have derived the 1D version of the rotor model as an effective description of continuum bosons. In doing so, they have established a connection between the strong disorder RG treatment of Altman, Kafri, Polkovnikov, and Refael and cold atom experiments on rubidium-87. Remarkably, the distributions that Vosk and Altman derive are of the same form as the fixed point distributions found by the strong disorder RG[13,20]. If such a treatment can be extended to the 2D case, that would be very valuable, both as a clarification of the critical behavior and as an indication of the relevance of the results to current experiments.

Appendix A: Sum Rule vs. Maximum Rule

In this appendix, we present a short argument for why it may be preferable to use the *sum rule* (see equations (32) and (33)) instead of the *maximum rule* (see equation (34)). In dimensions greater than one, it should be easier to form ordered (e. g. superfluid) phases. Indeed, the transition for the clean rotor model occurs when $\frac{J}{U}$ is substantially smaller than one[22]. Suppose we begin with the clean model at its critical point and then disorder it by increasing some Josephson couplings and decreasing some charging energies. Suppose further that we do this such that that the greatest Josephson coupling $J_{\max}$ is still less than the weakest charging energy $U_{\min}$. Then, using the maximum rule, the strong disorder renormalization procedure will predict no cluster formation at all. In other words, it will predict the ground state to be a Mott insulator, and this result seems inconsistent with the location of the clean transition. As mentioned previously, several authors have argued that, if $\frac{J_{\max}}{U_{\min}}$ exceeds the ratio $\frac{J}{U}$ at the clean transition, then we should expect glassy behavior, because there can be rare-regions in which the system looks locally superfluid[6]. With the sum rule, the procedure has a mechanism to circumvent this inconsistency. The Josephson coupling scale can actually grow through decimation and compete with the charging energy scale. Thus, there can be cluster formation, and the procedure can find ground states that are glassy or superfluid, even when all Josephson couplings of the bare model are less than the minimum bare charging energy. This indeed occurs in the numerics, as we have noted while presenting the numerical data above.

The notion of the Josephson coupling scale increasing through the RG may be a source of concern to some readers. The increase actually corresponds to the generation of multiple effective couplings between two sites through different paths in the lattice. This still happens when the maximum rule is used, but it is hidden through the discarding of certain paths. If the coupling through each path is treated as an independent Josephson coupling, then the Josephson coupling scale does decrease as the renormalization proceeds. However, when it is time to determine the next decimation step, it is necessary to consider all of the couplings between any two sites. For this reason, it makes sense to sum all the couplings into one effective coupling between the sites.

Appendix B: Measuring Physical Properties in the RG

Here, we work out two examples of how estimates of physical properties can be extracted from the RG procedure.

1. Particle Number Variance

First, consider the quantity:

$$\sum_j \langle \hat{n}_j^2 \rangle \tag{B1}$$

This particle number variance gives the mean squared number fluctuation away from the large filling, summed over all sites in the lattice. When normalized by $\frac{1}{L^2}$, we find numerically that this quantity stays constant as the system size is increased for all choices of distributions and parameters. As such, this quantity is completely uninteresting for discriminating between phases of the model, but we do calculate it for comparison to exact diagonalization in Appendix D.

The calculation of the particle number variance (B1) is most straightforward when clusters do not form, so let us first consider the case where some site X is not clustered with any other site during the renormalization. At some stage in the procedure, the site is decimated away. The number fluctuation on site X is locked to zero at leading order with corrections incorporated in second order perturbation theory. An approximation to the ground state value of $\langle \hat{n}_X^2 \rangle$ can be obtained from the perturbative expansion of the state. In particular:

$$\langle \hat{n}_X^2 \rangle \approx \frac{1}{2} \sum_k \frac{J_{Xk}^2}{(U_X + U_k)^2} \tag{B2}$$

When clusters do form, the calculation is trickier, but it can be performed by carefully keeping track of how the operator that we are targeting is written in terms of the cluster and relative number operators introduced in link decimation. To illustrate this, suppose we are trying to measure the operator:

$$\langle a_j \hat{n}_j^2 + a_k \hat{n}_k^2 \rangle = a_j \langle \hat{n}_j^2 \rangle + a_k \langle \hat{n}_k^2 \rangle \tag{B3}$$

The factors a_j and a_k are just numbers. In (B1), all these factors are one, but we will motivate the inclusion of more general a factors here shortly. If sites j and k are merged into a cluster, then we switch to the operators n_C and n_R to find:

$$a_j \hat{n}_j^2 + a_k \hat{n}_k^2 = \frac{a_j U_k^2 + a_k U_j^2}{(U_j + U_k)^2} \hat{n}_C^2 + \frac{a_j U_k - a_k U_j}{U_j + U_k} \hat{n}_R \hat{n}_C$$
$$+ (a_j + a_k) \hat{n}_R^2 \tag{B4}$$

During link decimation, the relative coordinate is specified, so the expectation value of the final term can be found immediately from the harmonic approximation:

$$(a_j + a_k) \langle \hat{n}_R^2 \rangle \approx (a_j + a_k) \frac{1}{2\gamma^{\frac{1}{2}}} \tag{B5}$$

Furthermore, the harmonic theory also predicts that the expectation value of the term linear in $\hat{n}_R$ will vanish. The calculation of the term proportional to $\hat{n}_C^2$ must be

deferred to later in the renormalization procedure. Thus, we keep the operator $\hat{n}_C^2$ in the portion of the sum (B1) that remains to be evaluated, where it appears just like the $\hat{n}^2$ for a bare site, but multiplied by a renormalized a_C coefficient. This was the motivation for including the a factors; though the bare values of these factors are all equal, different values can be generated through cluster formation. If the cluster is merged with another cluster in a future link decimation, we repeat the procedure above. When the cluster is finally decimated in a site decimation, the cluster's contributions to the sum (B1) are calculated through equation (B2) and then multiplied by the appropriate a factor.

The procedure outlined above can run into a difficulty that we can anticipate by thinking about the two-site problem. Suppose two sites, labelled 1 and 2, are connected by a Josephson coupling J_{12}. Furthermore, suppose $U_1 > U_2$, but both charging energies are greater than J_{12}. Then, we would decimate site 1 first and obtain an estimate for the site's contribution to the particle number variance (B1) through equation (B2). Next, we would decimate site 2 and find that it does not contribute at all to (B1) because there are no remaining links. However, the contribution of site 2 should, in fact, be equal to that of site 1, so our estimate is off by a factor of two. We can verify this by adopting cluster and relative coordinates (23) and then calculating (B1) by doing perturbation theory for the relative coordinate. To partially resolve this difficulty, we can keep track of which sites are unclustered by the RG process. At the end, we can return to the original lattice and calculate the contributions of these unclustered sites to (B1) using the bare couplings. For sites that *are* clustered by the RG, we reason that the main contribution to (B1) comes from internal fluctuations of the cluster, so this correction may not be so important.

It is possible to raise another objection to our calculation of (B1). The perturbation theory that leads to the result in (B2) incorporates the charging energies on sites neighboring site X. However, the perturbation theory leading to the RG rule (21) does not. How do we resolve this contradiction? When we calculate effective Josephson couplings in the RG, what we want to calculate is the effective rate of tunneling, once a boson has left one neighboring site and before it arrives at another, through the link-site-link system. For this purpose, it is appropriate to treat the sites neighboring site X as fictitious charging energy-free islands. On the other hand, when calculating observable quantities like (B1), it is important to account for the fact that the ability to move a particle or hole from site X to a neighboring site also depends on how hard it is to charge the neighboring site.

2. Susceptibility

In our studies of physical properties of the phases of the disordered rotor model, we considered the susceptibility χ. We defined this quantity in equation (41) as the linear response of the system to a uniform ordering field (40) coupling to $\cos(\hat{\phi}_j)$.

To calculate χ, we consider how to calculate the expectation value:

$$\sum_j b_j \langle \cos(\phi_j) \rangle \qquad (B6)$$

in the presence of an infinitesimal ordering field h. As with the a-factors in the calculation of the particle number variance, all the bare $b_j = 1$. When clusters form, the effective b-factor for the cluster can differ from unity.

If a bare site is decimated, then perturbation theory in h gives:

$$\langle \cos(\phi_X) \rangle = \frac{h}{U_X} \qquad (B7)$$

Since $b_X = 1$ for a bare site, (B7) is the contribution of site X to the quantity (B6).

When a link decimation joins two sites into a cluster, the corresponding terms in the sum (B6) merge as:

$$
\begin{aligned}
b_j \cos(\hat{\phi}_j) + b_k \cos(\hat{\phi}_k) &= b_j \cos(\hat{\phi}_C + \mu_j \hat{\phi}_R) \\
&\quad + b_k \cos(\hat{\phi}_C - \mu_k \hat{\phi}_R) \\
&\approx b_j \cos(\hat{\phi}_C) \langle \cos(\mu_j \hat{\phi}_R) \rangle \quad (B8) \\
&\quad - b_j \sin(\hat{\phi}_C) \langle \sin(\mu_j \hat{\phi}_R) \rangle \\
&\quad + b_k \cos(\hat{\phi}_C) \langle \cos(\mu_k \hat{\phi}_R) \rangle \\
&\quad + b_k \sin(\hat{\phi}_C) \langle \sin(\mu_k \hat{\phi}_R) \rangle \\
&= (b_j c_{DW,j} + b_k c_{DW,k}) \cos(\hat{\phi}_C)
\end{aligned}
$$

In this calculation, μ_j and μ_k are the ratios introduced in equation (30), and $c_{DW,j}$ and $c_{DW,k}$ are precisely the Debye-Waller factors given in equation (31). We can read off the renormalized b-factor for the cluster from the calculation above, and the resulting expression is given in equation (42).

Next, it is important to note that the ordering field terms in the Hamiltonian (40) transform in the same way. In other words, the term coupling to $\cos(\hat{\phi}_C)$ in the Hamiltonian should appear multiplied by b_C after a merger. Physically, this corresponds to the fact that, when the cluster phase rotates, s_C bare phases rotate semi-coherently. Complete coherence is lost due to quantum fluctuations, which are accounted for by Debye-Waller factors. The factor b_C can be thought of as the effective number of rotors that are coherently ordering with the field. The energetic cost of ϕ_C straying from the direction of the ordering field is therefore amplified by this factor. When the cluster is finally decimated, the perturbation is amplified by this amount. Furthermore, $\cos(\hat{\phi}_C)$ appears in the sum (B6) multiplied by b_C, so the total contribution of the cluster to the sum is:

$$b_C \langle \cos(\phi_C) \rangle = \frac{h b_C^2}{U_C} \qquad (B9)$$

From equations (B7) and (B9), the calculation of the linear response to an infinitesimal h (i.e. the susceptibility χ) follows immediately.

Appendix C: The $P_i(U)$ Gaussian, $P_i(J)$ Power Law Data Set

In the work reported above, we have explored the superfluid-insulator transition of the disordered rotor model using several different species of disorder (see equations (9)-(12)). In doing so, we have exposed universal features of the critical behavior. After providing numerical evidence of this universality however, we focus on data for one particular choice of initial distributions. In this appendix, we describe this choice of distributions in greater detail.

The choice of distributions in question first appears in Figure 7. The initial distribution of charging energies $P_i(U)$ is taken to be a Gaussian with center at U_0 and width $\sigma_U = 2$. Hence, the form of the distribution is:

$$P_i(U) \propto \exp\left[-\frac{(U-U_0)^2}{8}\right] \tag{C1}$$

Recall that the Gaussian distribution is truncated at $3\sigma_U = 6$, so the distribution only has weight in the interval $U \in (U_0 - 6, U_0 + 6)$. We leave U_0 unspecified for the moment, because it is the parameter that we use to tune through the transition.

The initial Josephson coupling distribution $P_i(J)$ is a power law of the form $J^{-1.6}$. We choose the cutoffs so that the distribution has weight for $J \in (0.5, 100)$. This is a very wide power law distribution, so the corresponding flows begin well above the unstable finite disorder fixed point in the numerical flow diagrams. Explicitly:

$$P_i(J) \approx 0.413 J^{-1.6} \tag{C2}$$

For this choice of distributions, we have acquired data for $U_0 = 400, 20, 18, 16, 14, 12, 10, 9.8, 9.6, 9.4, 9.2, 8.8, 8.6, 8.4, 8.2, 8, 7.5, 7,$ and 6.5. To more finely target the transition, we have probed the interval $9.1 \geq U_0 \geq 8.9$ in increments of 0.01. We have always acquired data for $L = 25, 50, 75, 100, 150, 200,$ and 300. In all cases, we have pooled data for 10^3 disorder samples. The peak in the data for s_2 vs. U_0 gives the following estimate of the critical point:

$$U_{0,c} \approx 8.97 \pm 0.02 \tag{C3}$$

Close to criticality, it is better to use a lower value of the thresholding parameter α. For several values of U_0 such that $10 \geq U_0 \geq 8$, we have run the RG with $\alpha_h = 10^{-5}$ and $\alpha_\ell = 5 \times 10^{-6}$ to test for convergence. Further away from criticality, we have instead used $\alpha_h = 5 \times 10^{-5}$ and $\alpha_\ell = 2.5 \times 10^{-5}$. Figure 22 shows a test of the convergence of the maximum cluster size $s_{\max}$ in the thresholding parameter α. We plot:

$$v = \frac{s_{\max}(\alpha_h)}{s_{\max}(\alpha_\ell)} \tag{C4}$$

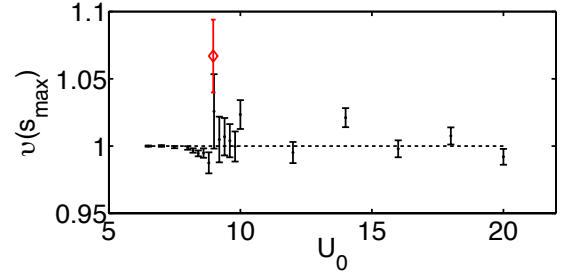FIG. 22: A test of the convergence of $s_{\max}$ in the thresholding parameter α. The variable v is the ratio of the estimate of $s_{\max}$ for α_h, the less conservative value of the thresholding parameter, to α_ℓ, the more conservative value. We plot v against the tuning parameter U_0. The closest data point to criticality ($U_0 = 8.97$) is indicated with a diamond. Note that $v > 1$ typically indicates convergence since less conservative thresholding (higher α) corresponds to throwing away more bonds and, therefore, biases the system away from cluster formation. Smaller values of α_h and α_ℓ are used in the vicinity of the transition. See the text of Appendix C for details.

vs. the tuning parameter U_0. The ratio (C4) is essentially always within two error bars of unity. We take this as an indication that physical properties have converged.

Appendix D: Further Comments on the Use of the Strong Disorder RG in a Finite Disorder Context

This appendix is devoted to exploring, in further detail, the validity of the RG procedure. We first expand upon the argument, introduced earlier in the paper, for the reliability of the RG near criticality. Then, we move away from criticality and assess the performance of the RG in the various phases of the disordered rotor model (7). Next, we focus on each of the RG steps, consider circumstances in which they may fail to capture important physics, and formulate tests to ensure that the RG is trustworthy in these situations. Finally, we present a comparison of the RG to exact diagonalization of small systems.

1. Review of the Argument for the RG at Criticality

Our confidence in the RG procedure near criticality rests on the form of the critical Josephson coupling distribution, reported in equations (36) and (39). Infinite randomness develops when $P(J) \propto J^{-1}$, and our numerical evidence suggests that the critical distribution of the disordered rotor model decays even more strongly[19]. Nevertheless, the critical distribution does not exhibit infinite randomness, because as seen in Figure 11, it is cut off from below. Recall that the lower cutoff of the "Josephson coupling distribution" is set by our choice to retain, *in statistics*, only the dominant $2\tilde{N}$ Joseph-

son couplings, where $\tilde{N}$ is the number of sites remaining in the effective lattice. Then, the appropriate way to interpret the distributions in Figure 10 is the following: penetrating any given site in the effective lattice, there are likely to be on the order of four Josephson couplings drawn from the depicted distribution. There may be other links penetrating the site, but these will be even weaker. We can estimate the typical strength of the four dominant links by comparing the median of the critical Josephson coupling distribution to the maximum. For the closest approach to criticality with the initial distributions described in Appendix C, we find that the ratio $\frac{J_{\text{typ}}}{\Omega}$ is approximately 0.11 ± 0.01 near the fixed point. Hence, the typical link is quantitatively weak compared to $\frac{J}{U} \approx 0.345$ at the clean transition[22].

The considerations above form a strong argument for the validity of the site decimation RG step. Here, we seek out the dominant effective charging energy in the effective lattice, and treat the links penetrating the site in perturbation theory. This perturbation theory is likely a very good approximation, because the Josephson couplings penetrating the site in question are usually extremely weak.

Now, we turn to the link decimation step, in which we seek out the largest Josephson coupling in the lattice and merge the corresponding sites into a cluster. Although, the Josephson coupling being decimated is the largest energy scale in the system, there is a high probability that all the other links penetrating the two sites being joined will be very small. However, the critical distribution of charging energies is *not* peaked at low U. The structure of the distributions plotted in Figure 12 suggests that it is quite likely that one or both sites being merged will have a charging energy of the same order as the RG scale, thus violating the strong disorder hypothesis. Our treatment of the quantum fluctuations of the relative phase of the cluster is based on the harmonic approximation (27). Is this approximation appropriate when the charging energies of the two-site problem are comparable in magnitude to the Josephson coupling? Alternatively, do the quantum fluctuations grow so large that the clustering becomes meaningless? We address this question as follows: using the fact that the remaining links are weak, we isolate the two site problem and solve it exactly, treating the remaining links via second order perturbation theory. Comparing the results of the RG with the exact solution, we find that, even in this worst case scenario, the RG produces reasonably accurate effective couplings. The evidence for this claim is given in section 3 below.

2. Reliability of the RG in the Phases

How reliable is the RG when we move away from criticality and into the phases of the disordered rotor model? To gain some insight into this question, we can consult Figure 23, which expands upon Figures 11 and 13 by plotting renormalized J and U distributions away from
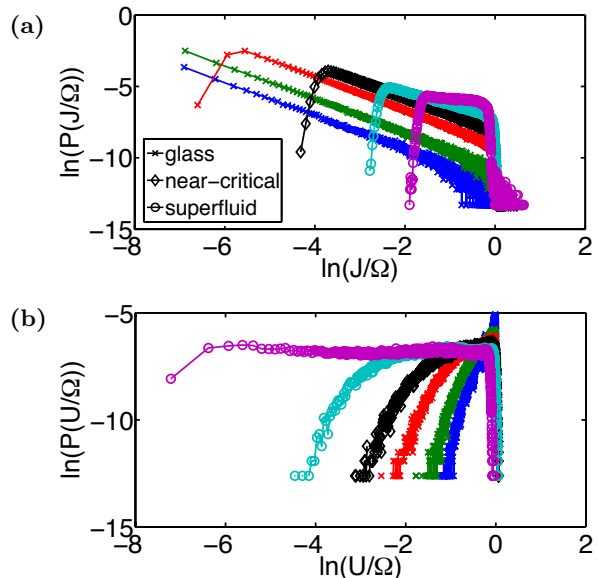
criticality.

FIG. 23: In panel (a), a sweep of renormalized J distribution through the glass and into the superfluid. The initial distributions are those described in Appendix C: $P_i(U)$ is Gaussian and $P_i(J) \propto J^{-1.6}$. All data is taken for $L = 300$ lattices, and the renormalized distribution is computed when 300 sites remain in the effective lattice. The values of U_0 shown are 18, 12, 9.6, 8.97 (near-critical), 8.4, and 7.5. Panel (b) shows the corresponding sweep of the renormalized U distribution at the same stage of the RG.

Proceeding into the glassy regime, the arguments presented above for the validity of the RG near criticality generally become stronger. The primary reason for this is that the renormalized J distributions become progressively broader than at criticality. In the flow diagrams (Figures 6-9), this is reflected in the apparent divergence of $\frac{\Delta J}{\bar{J}}$. Consequently, the assumption of isolating local degrees of freedom becomes better as we get deeper into the glass. One complication is that the renormalized U distribution becomes more strongly peaked near the RG scale. This may pose trouble for the link decimation step and makes it especially important to consider the reliability of this step when a strong J_{jk} couples two sites with charging energies $U_j \approx U_k \approx J_{jk}$. As mentioned previously, we will study this worst-case scenario in part 3 of this appendix and find that the RG still works reasonably well.

Now, we turn to the superfluid phase. As we proceed away from criticality, the renormalized charging energy distribution becomes flatter and broader. The broadening of this distribution implies that the likelihood of encountering a strong Josephson coupling that connects sites with comparably strong charging energies decreases as we get deeper into the superfluid phase. However, the J distribution *also* seems to become flat deep in the superfluid, and this is problematic. For example, during link decimation, it may not be a reasonable approx-

imation to isolate the two-site problem centered on the strongest Josephson coupling. As we proceed into the superfluid, it is necessary to be more dubious of the RG results; nearer to criticality however, the arguments used at the critical point are probably approximately valid.

The plots in Figure 23 attempt to elucidate systematics in the behavior of the renormalized distributions in the insulating and superfluid regimes, but we should mention that this figure should be interpreted with some care. For the choice of distributions in Appendix C, flows terminating in the insulating or superfluid regions of the flow diagram nevertheless propagate in the vicinity of the unstable fixed point along the way. This can be seen, for instance, in Figure 7. For certain choices of initial distributions, there can be flows towards the insulating or superfluid regimes which never propagate anywhere near the unstable fixed point. Consequently, the RG never has an opportunity to wash away the details of the initial distributions and allow the universal properties of the fixed point to emerge. Hence, the renormalized distributions generated along such flow trajectories are unlikely to exhibit the clean systematic properties seen in Figure 23.

3.   Analysis of Potential Problems with the RG

Next, we address some potential difficulties with the arguments presented above for the reliability of the renormalization procedure in the critical region. These difficulties are rooted in the lack of strong randomness in the critical charging energy distribution.

Consider the lattice geometry shown in Figure 24. Suppose that all links except the Josephson coupling between sites 1 and 2 are perturbatively weak. Now, suppose further that J_{12}, U_1, and U_2 are comparable in magnitude, but J_{12} is the largest of the three. We would like to formulate a test of whether the RG appropriately handles this situation. Within the RG, a link decimation would merge sites 1 and 2 into a cluster. All links penetrating sites 1 and 2 would be modified by their corresponding Debye-Waller factors (31) $c_{\mathrm{DW},1}$ and $c_{\mathrm{DW},2}$. Then, because all the remaining links are assumed to be very weak, the cluster of sites 1 and 2 will be decimated, producing an effective coupling between sites 3 and 5:

$$\tilde{J}_{35,RG} = c_{\mathrm{DW},1} c_{\mathrm{DW},2} \frac{J_{13} J_{25}(U_1 + U_2)}{U_1 U_2} \qquad (D1)$$

Another approach to calculating this effective coupling would be the following: take the two-site problem of sites 1 and 2 and exactly diagonalize it. Then, to leading order, sites 1 and 2 should be locked into the two-site ground state, with perturbative corrections coming from the Josephson couplings J_{13}, J_{14}, and J_{25}. This perturbation theory leads to an effective coupling through the sites 1 and 2. This alternative procedure is perhaps more appropriate, because it does not presuppose the harmonic approximation. In Figure 25, we assess how much of an
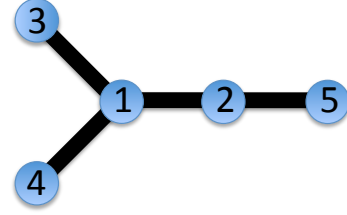

FIG. 24: The graph structure for the tests reported in Figures 25 and 26. The links J_{13}, J_{14}, and J_{25} are assumed to be perturbatively weak. The charging energies U_1 and U_2 and the Josephson coupling J_{12} are varied to explore potentially troublesome scenarios.

error we make by adopting the harmonic approximation. Holding J fixed, we sweep $U = U_1 = U_2$ through J, comparing the RG with the alternative method outlined above. We see that the usual RG performs reasonably well, implying that the harmonic approximation is safe.

Finally, we consider another potentially dangerous scenario. We return to the lattice shown in Figure 24. Now, we assume that J_{12} is greater than all other Josephson couplings, but it too is much weaker than the charging energies U_1 and U_2. In particular, $\frac{J_{12}}{U_2} = 0.05$. Then, we sweep U_1 such that it passes through a regime where $|U_1 - U_2| < J_{12}$. The danger here is that the RG may ignore resonance effects associated with this region. Within the usual RG, sites 1 and 2 will be decimated in turn to give:

$$\tilde{J}_{35,\mathrm{RG}} \approx \frac{J_{13} J_{12} J_{25}}{U_1 U_2} \qquad (D2)$$

$$\tilde{J}_{34,\mathrm{RG}} \approx \frac{J_{13} J_{14}}{U_1} \qquad (D3)$$

where we ignore subleading corrections coming from potential applications of the sum rule, depending on the order of decimation of sites 1 and 2. To consider potential resonance effects, we can also implement the same hybrid exact diagonalization and RG procedure that we used above. In Figure 26, we compare the two methods and find excellent agreement.

4.   Strong Disorder RG vs. Exact Diagonalization

As a final test of the RG procedure, we now compare the RG to exact diagonalization of small systems. We truncate the possible number fluctuation on each site to $n_j = -1, 0, 1$, interpret these three values as possible z-axis spin projections of a spin-one object, and in doing so, arrive at a "spin-one" model:

$$\hat{H} = -\sum_{\langle jk \rangle} \frac{J_{jk}}{2}(\hat{S}_j^+ \hat{S}_k^- + \hat{S}_j^- \hat{S}_k^+) + \sum_j U_j \hat{S}_{zj}^2 \qquad (D4)$$
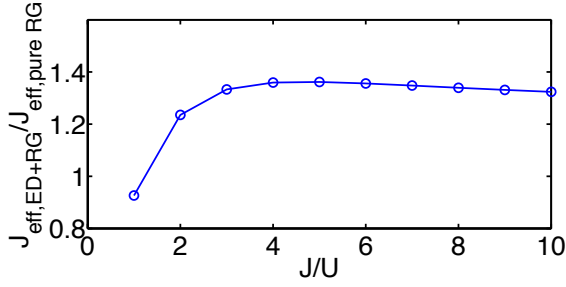
FIG. 25: In this test, $J = J_{12}$ is assumed to be the strongest coupling in the system, but $U = U_1 = U_2$ may be of the same order. An effective coupling between sites 3 and 5 is calculated using two methods. One is the usual RG scheme used in this paper. Another is a hybrid exact diagonalization and RG scheme: The two-site problem of sites 1 and 2 is exactly diagonalized. Then, the resulting cluster is decimated away, and perturbation theory is used to calculate an effective coupling between sites 3 and 5. The two candidate values for the effective coupling J_{35} are compared in the plot, as a function of $\frac{J}{U}$.
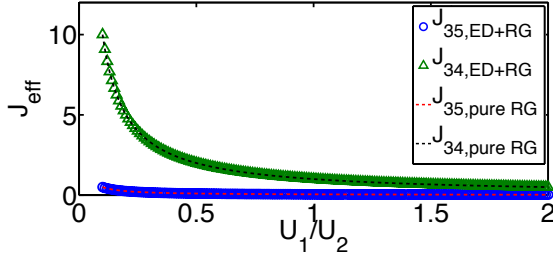

FIG. 26: In this test, $J_{12} = 0.05$ and $U_2 = 1$. Hence, J_{12} is relatively quite weak. However, we vary U_1 such that it passes through a regime where $|U_1 - U_2| < J_{12}$, where there may be a danger of resonance effects. We calculate the effective couplings J_{34} and J_{35} using two schemes. One is the usual RG scheme used in this paper. Another is a hybrid exact diagonalization and RG scheme: the two-site problem of sites 1 and 2 is exactly diagonalized. Then, the resulting cluster is decimated away, and perturbation theory is used to calculate an effective coupling between sites 3 and 4 and between sites 3 and 5. The effective couplings predicted by the two methods are compared in the plot, as a function of $\frac{U_1}{U_2}$. No resonance effects are observed.
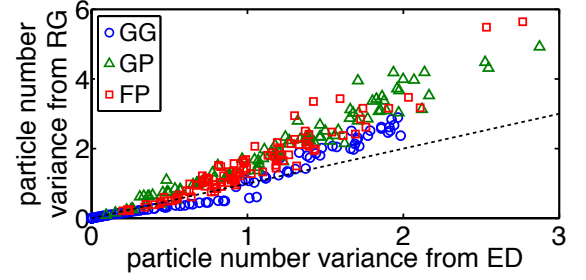

FIG. 27: A sample-by-sample comparison of the particle number variance predictions from exact diagonalization and from the renormalization procedure. The disordered couplings are drawn from three different choices of the distributions, with 100 samples per distribution type. See the text of Appendix D for details on the distribution choices GG, GP, and FP. Also pictured is the coincidence line $y = x$, along which the points would ideally fall for full quantitative agreement.
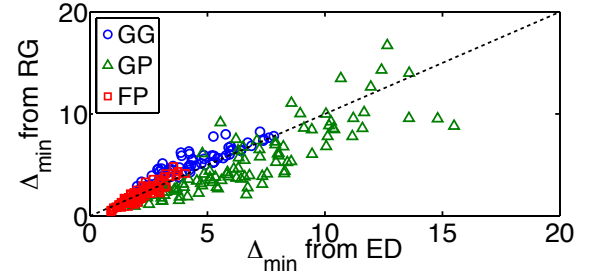

FIG. 28: Same as Figure 27, but the quantity being compared is the charging gap $\Delta_{\min}$.

The Hilbert space of this spin-one model grows with the size of the lattice as 3^{L^2}. The particle number conservation of the rotor model manifests here as total spin conservation along the z-axis. This means that we can partition the Hilbert space into different total spin sectors and diagonalize the sectors separately. For most ground state expectation values, we just need to diagonalize the total spin zero sector, and to calculate a charging gap, the only additional diagonalization needed is for the total spin one sector. Despite these simplifications, computational limitations restrict us to studying 3×3 lattices using CLAPACK. Testing the RG against exact diagonalization cannot directly tell us about the reliability of the RG at criticality, because exact diagonalization is limited to very small system sizes. However, a comparison with exact diagonalization *can* tell us how well the RG captures information about small patches of a larger lattice, and this information is potentially quite valuable for building confidence in the RG.

Another complication arises precisely due to the Hilbert space truncation: the spin-one model may not always approximate the full rotor model well. This is especially true when there is cluster formation, because then the rotor model has more of an opportunity to access particle number fluctuations that exceed 1 in magnitude.

In other words, the strong disorder renormalization group and the exact diagonalization of the spin-one model constitute *different* approximations to the behavior of our random boson model. We cannot expect the two approximations to show full quantitative agreement, but we proceed with the comparison, despite its limitations, with the hope of at least seeing qualitative correspondence between the two methods.

Our general approach to comparing the RG with exact diagonalization will be to measure physical quantities, on individual 3×3 samples, using both methods and assess if there is a correlation between the predictions. The first quantity that we compare is the particle number variance (B1). The interested reader may consult Appendix B to see how this quantity is calculated during the renormalization procedure. We also compare the charging gap $\Delta_{\min}$, the minimum energy needed to add a particle or hole to the system. This quantity is typically estimated during site decimation. The logic behind site decimation is that the charging energy for some site X is greater than all other scales in the problem, so the site can be disconnected from the rest of the lattice to leading order. Then, the charging energy gives an estimate for the local charging gap on that site. During the RG, we find many such charging gaps from the various site decimations. The minimum among all of these gives an estimate for the charging gap for the whole system. This minimum is always given by the charging energy of the final remaining site, so an estimate of $\Delta_{\min}$ can be simply obtained by renormalizing down to a single site problem and measuring the charging energy of the remaining site. For the purposes of comparison to exact diagonalization however, we find that we obtain better quantitative agreement between the two methods if we renormalize down to an effective two-site problem and then perform exact diagonalization on that system. Exactly diagonalizing the $n_{\text{tot}} = 0$ and $n_{\text{tot}} = 1$ sectors of this two-site problem then yields a charging gap for the system. In this exact diagonalization, we need not truncate the on-site number fluctuation to $n_X = -1, 0, 1$. Instead, in the numerics, we typically truncate to $n_X = -100 \ldots 100$.

In Figures 27 and 28, we present comparisons for three different data sets. In the first data set, we use take $P_i(U)$ and $P_i(J)$ to be Gaussian. We fix $U_0 = 10$ and $\sigma_U = 3$. Then, we randomly sample J_0 in the interval $(0, 5)$ and σ_J in the interval $(0, \frac{J_0}{3})$. The aim is to approximate some of the environments that the RG encounters in runs such as those reported in Figure 6. The second data set uses the distributions described in Appendix C: $P_i(U)$ is Gaussian and $P_i(J) \propto J^{-1.6}$. We randomly sample $U_0 \in (6.5, 20)$. Here, the motivation is to look at the types of environments that the RG encounters when it approaches the unstable fixed point from above. In the final data set, we try to mimic 3×3 patches that the RG might encounter near criticality. To this end, the initial J distribution is fixed to a power law $P(J) \propto J^{-1.16}$ (see equation (39)) and the cutoffs are chosen so that the ratio of $J_{\min}$ to $J_{\max}$ is approximately that observed in

panel (b) of Figure 13. The distribution $P_i(U)$ is flat with $U_{\max} = J_{\max}$ and with $U_{\min}$ randomly sampled such that the ratio of $U_{\min}$ to $U_{\max}$ lies in (e^{-2}, e^{-1}). Figures 27 and 28 identify these three data sets with the labels GG, GP, and FP respectively.

Both figures show that the predictions of the RG are clearly correlated with the predictions from exact diagonalization, although the level of quantitative correspondence varies. For the particle number variance, quantitative agreement is lost at higher values of the variance, essentially corresponding to cases in which there is clustering. One potential source of error could be the Hilbert space truncation of the exact diagonalization, although the structure of the harmonic ground state (27) makes it unlikely that this could account for the entire discrepancy. Nevertheless, these comparisons suggest that the RG is retaining useful information about the system.

[1] B. Crooker, B. Hebral, E. Smith, Y. Takano, and J. Reppy, Physical Review Letters. **51**, 666 (1983).

[2] J. Reppy, Physica B+C. **126**, 335 (1984).

[3] P. Weichman, Arxiv Preprint arXiv:0810.3263. (2008).

[4] M. Fisher, P. Weichman, G. Grinstein, and D. Fisher, Physical Review B. **40**, 546 (1989).

[5] T. Giamarchi and H. Schulz, Physical Review B. **37**, 325 (1988).

[6] L. Pollet, N. Prokofev, B. Svistunov, and M. Troyer, Physical Review Letters. **103**, 140402 (2009).

[7] M. Greiner, O. Mandel, T. Esslinger, T. Hänsch, and I. Bloch, Nature. **415**, 39 (2002).

[8] T. Schulte, S. Drenkelforth, J. Kruse, W. Ertmer, J. Arlt, K. Sacha, J. Zakrzewski, and M. Lewenstein, Physical Review Letters. **95**, 170411 (2005).

[9] L. Fallani, J. Lye, V. Guarrera, C. Fort, and M. Inguscio, Physical Review Letters. **98**, 130404 (2007).

[10] J. Billy, V. Josse, Z. Zuo, A. Bernard, B. Hambrecht, P. Lugan, D. Clément, L. Sanchez-Palencia, P. Bouyer, and A. Aspect, Nature **453**, 891 (2008).

[11] M. White, M. Pasienski, D. McKay, S. Zhou, D. Ceperley, and B. DeMarco, Physical Review Letters. **102**, 55301 (2009).

[12] T. Giamarchi, P. Le Doussal, and E. Orignac, Physical Review B. **64**, 245119 (2001).

[13] E. Altman, Y. Kafri, A. Polkovnikov, and G. Refael, Physical Review Letters. **93**, 150402 (2004).

[14] E. Altman, Y. Kafri, A. Polkovnikov, and G. Refael, Physical Review B. **81**, 174528 (2010).

[15] P. Weichman and R. Mukhopadhyay, Physical Review B. **77**, 214516 (2008).

[16] C. Dasgupta and S. Ma, Physical Review B. **22**, 1305 (1980).

[17] R. Bhatt and P. Lee, Physical Review Letters. **48**, 344 (1982).

[18] D. Fisher, Physical Review B. **50**, 3799 (1994).

[19] D. Fisher, Physica A: Statistical Mechanics and its Applications. **263**, 222 (1999).

[20] R. Vosk and E. Altman, Arxiv Preprint arXiv:1104.2063. (2011).

[21] C. Bruder, R. Fazio, and G. Schön, Annalen der Physik. **14**, 566 (2005).

[22] N. Teichmann, D. Hinrichs, M. Holthaus, and A. Eckardt, Physical Review B. **79**, 100503 (2009).

[23] A. Gottlob and M. Hasenbusch, Physica A: Statistical Mechanics and its Applications **201**, 593 (1993).

[24] A. Harris, Journal of Physics C: Solid State Physics. **7**, 1671 (1974).

[25] T. Vojta, Journal of Low Temperature Physics. **161**, 299 (2010).

[26] I. Kovács and F. Iglói, Physical Review B. **82**, 054437 (2010).

[27] O. Motrunich, S. Mau, D. Huse, and D. Fisher, Physical Review B. **61**, 1160 (2000).

[28] D. Stauffer and A. Aharony, *Introduction to Percolation Theory.* (Taylor & Francis, London, 1994).

[29] U. Bissbort and W. Hofstetter, EPL. **86**, 50007 (2009).

[30] F. Krüger, S. Hong, and P. Phillips, Arxiv Preprint arXiv:1006.2395. (2010).

[31] D. Huse, Private communication. (2011).

[32] N. Prokofev and B. Svistunov, Physical Review Letters. **92**, 15703 (2004).

[33] T. Roscilde and S. Haas, Physical Review Letters. **99**, 47205 (2007).

[34] P. Sengupta and S. Haas, Physical Review Letters. **99**, 50403 (2007).

[35] R. Fernandes and J. Schmalian, Physical Review Letters. **106**, 67004 (2011).

[36] N. Bray-Ali, J. Moore, T. Senthil, and A. Vishwanath, Physical Review B **73**, 064417 (2006).

[37] L. Wang and A. Sandvik, Physical Review Letters. **97**, 117204 (2006).

[38] L. Wang and A. Sandvik, Physical Review B **81**, 054417 (2010).

[39] A. Sandvik, Physical Review Letters. **96**, 207201 (2006).

[40] J. Moore, Private communication. (2011).

[41] K. Bouadim, Y. Loh, M. Randeria, and N. Trivedi, Arxiv preprint arXiv:1011.3275. (2010).

[42] R. Crane, N. Armitage, A. Johansson, G. Sambandamurthy, D. Shahar, and G. Grüner, Physical Review B. **75**, 184530 (2007).

[43] A. Frydman, O. Naaman, and R. Dynes, Physical Review B. **66**, 052509 (2002).

[44] D. Sherman, G. Kopnov, D. Shahar, and A. Frydman, Arxiv preprint arXiv:1112.0776. (2011).

[45] A. Allain, Z. Han, and V. Bouchiat, Arxiv preprint arXiv:1109.6910. (2011).

[46] R. Yu, L. Yin, N. Sullivan, J. Xia, C. Huan, A. Paduan-Filho, N. Oliveira, S. Haas, A. Steppke, C. Miclea, et al., Arxiv Preprint arXiv:1109.4403. (2011).

[47] Y. Wang, W. Guo, and A. Sandvik, Arxiv preprint arXiv:1110.3213. (2011).